Measurement of the Neutron Magnetic Form Factor at High Q^2 Using the Ratio Method on Deuterium

A New Research Proposal to the Jefferson Lab Program Advisory Committee (PAC32)

G.P. Gilfoyle*†
University of Richmond

W.K. Brooks*, S.Stepanyan
Jefferson Lab

M.F. Vineyard*
Union College

S.E. Kuhn, J.D. Lachniet*, L.B. Weinstein
Old Dominion University

K. Hafidi*, J.Arrington, D.Geesaman, R.Holt,
D.Potterveld, P.E.Reimer, P.Solvignon
Argonne National Laboratory

M. Holtrop
University of New Hampshire

M. Garçon
DAPNIA/SPhN-Saclay

Theory Support

S. Jeschonnek
Ohio State University

P. Kroll
Universität Wuppertal

* Co-spokesperson.
† Contact person.

July 17, 2007

Abstract

We propose to measure the magnetic form factor of the neutron using the 11 GeV electron beam in the upgraded CEBAF and CLAS12 detector. The measurement will cover the range $Q^2 = 2 - 14$ GeV^2. The neutron's magnetic form factor is one of the fundamental quantities of nuclear physics and its value is an important constraint for the newly-developed generalized parton distributions that hold the promise of dramatically expanding our understanding of the nucleon. The form factors are also important challenges for lattice QCD to meet. This measurement is part of a broad assault on the four, elastic, electromagnetic, nucleon form factors at Jefferson Lab. We will use the ratio of quasielastic $e-n$ to quasielastic $e-p$ scattering on deuterium. The ratio method is less vulnerable to uncertainties than previous methods and we will have consistency checks between different detector components and an overlap with our previous CLAS measurements. Precise measurements of G_M^n have already been made by our group and others at lower Q^2. This experiment can be done with the base equipment for CLAS12. The groups behind this project have made significant commitments to the Jefferson Laboratory 12-GeV Upgrade.

Contents

1 Introduction

The internal structure of the nucleon represents a fundamental challenge for nuclear physics. The elastic electromagnetic form factors are the most basic observables that describe this internal structure and their evolution with Q^2 characterizes the distributions of charge and magnetization within the proton and neutron. These observables also provide stringent tests of non-perturbative QCD and are connected to generalized parton distributions (GPDs) via the appropriate sum rules. We propose to extend our successful measurements of the neutron magnetic form factor G_M^n to the higher Q^2 that will be available with the 12-GeV Upgrade of CEBAF. We will use the ratio of the quasielastic electron-neutron to electron-proton scattering on deuterium to extract a precise ($\approx 3\%$) measurement of G_M^n. In Section 2 we present more details on the scientific motivation for measuring G_M^n and review the world's data for this quantity. In Section 3 we outline the method for making the measurement, estimate the expected quality of the data, and discuss the relationship of this experiment to others at JLab. We list the commitments of the co-spokespersons and supporters in Section 4 and draw conclusions in Section 5. In Table 1 we summarize the commitment of the experimental collaborators to the Jefferson Lab 12-GeV Upgrade.

2 Scientific Motivation

The nucleon elastic form factors are defined through the matrix elements of the electromagnetic current $J_\mu = \overline{\psi}\gamma_\mu\psi$ as

$$\langle N(P')|J_\mu(0)|N(P)\rangle = \overline{u}(P')\left(\gamma_\mu F_1(Q^2) + \frac{i\sigma_{\mu\nu}q^\nu\kappa}{2M}F_2(Q^2)\right)u(P) \tag{1}$$

where P and P' are the initial and final nucleon momenta, $q = P - P'$, $Q^2 = -q^2$, M is the nucleon mass, κ is the anomalous magnetic moment, and F_1 and F_2 are scalar functions of Q^2 that characterize the internal structure of the nucleon. These are the Dirac and Pauli form factors, respectively. The differential cross section for elastic electron-nucleon scattering can then be calculated in the laboratory frame as [1]

$$\frac{d\sigma}{d\Omega} = \sigma_{Mott}\left[\left(F_1^2 + \frac{\kappa^2Q^2}{4M^2}F_2^2\right) + \frac{Q^2}{2M^2}\left(F_1 + \kappa F_2\right)^2\tan^2\left(\frac{\theta}{2}\right)\right] \tag{2}$$

where θ is the electron scattering angle, κ is the nucleon anomalous magnetic moment, and σ_{Mott} is

$$\sigma_{Mott} = \frac{\alpha^2E'\cos^2(\frac{\theta}{2})}{4E^3\sin^4(\frac{\theta}{2})} \quad . \tag{3}$$

It is preferable to define different electromagnetic form factors that are related to the charge and magnetization density of the nucleon in the appropriate kinematics. These so-called Sachs form factors are defined as

$$G_E = F_1 - \frac{\kappa Q^2}{4M^2}F_2 \qquad G_M = F_1 + \kappa F_2 \tag{4}$$

Name	Institution	Project
G.P. Gilfoyle	University of Richmond	Software for event simulation and online/offline reconstruction.
M.F. Vineyard	Union College	Software for analysis, simulation, and controls.
S. Stepanyan, W.K. Brooks	JLab	Group leader for the electromagnetic calorimeters for CLAS12.
L.B. Weinstein, S.E. Kuhn, J.D. Lachniet	Old Dominion University	Construction of Region 1 drift chambers.
K. Hafidi, J.Arrington, D.Geesaman, R.Holt, D.Potterveld, R.Reimer, P.Solvignon	Argonne National Lab	Design, prototyping, construction, and testing of the new high-threshold Cerenkov counter.
M. Holtrop	University of New Hampshire	Software for simulation and design, prototyping, construction, and testing of the silicon vertex detector.
M. Garcon	DAPNIA/SPhN-Saclay	Design, prototyping, construction, and testing of the central tracker.

Table 1: Summary of commitments (subject to funding approval) of CLAS collaborators on this proposal to the Jefferson Lab, 12-GeV Upgrade.

so Equation 2 can be written as

$$\frac{d\sigma}{d\Omega} = \sigma_{Mott}\left(G_E^2 + \frac{\tau}{\epsilon}G_M^2\right)\left(\frac{1}{1+\tau}\right) \tag{5}$$

where

$$\tau = \frac{Q^2}{4M^2} \qquad \text{and} \qquad \epsilon = \frac{1}{1+2(1+\tau)\tan^2(\frac{\theta}{2})} \quad . \tag{6}$$

The current status of our understanding of G_M^n is shown in Figure 1 where G_M^n is scaled by the dipole form factor $G_D(Q^2) = 1/(1+Q^2/\Delta)^2$ and $\Delta = 0.71$ (GeV/c)^2. The parameter Δ is interpreted as the square of the effective meson mass. We focus here on Q$^2 > 1.0$ GeV^2 where the neutron magnetic form factor agrees with the dipole form within 5-10%. This agreement can be qualitatively understood as a virtual photon interacting with the nucleon after the photon has fluctuated into a vector meson. There are, however, deviations from the dipole form that invite investigation. Some of the data have large error bars due largely to uncertainties in subtracting the contribution of the proton in these measurements using inclusive quasielastic scattering on deuterium [2]. The more precise measurements including

the recent work by Lachniet, *et al.* and the CLAS E5 group (the red circles in Figure 1) [3, 4] and others [5, 6, 7, 8] use a ratio method that we propose to extend to higher Q^2 and which is described in Section 3.

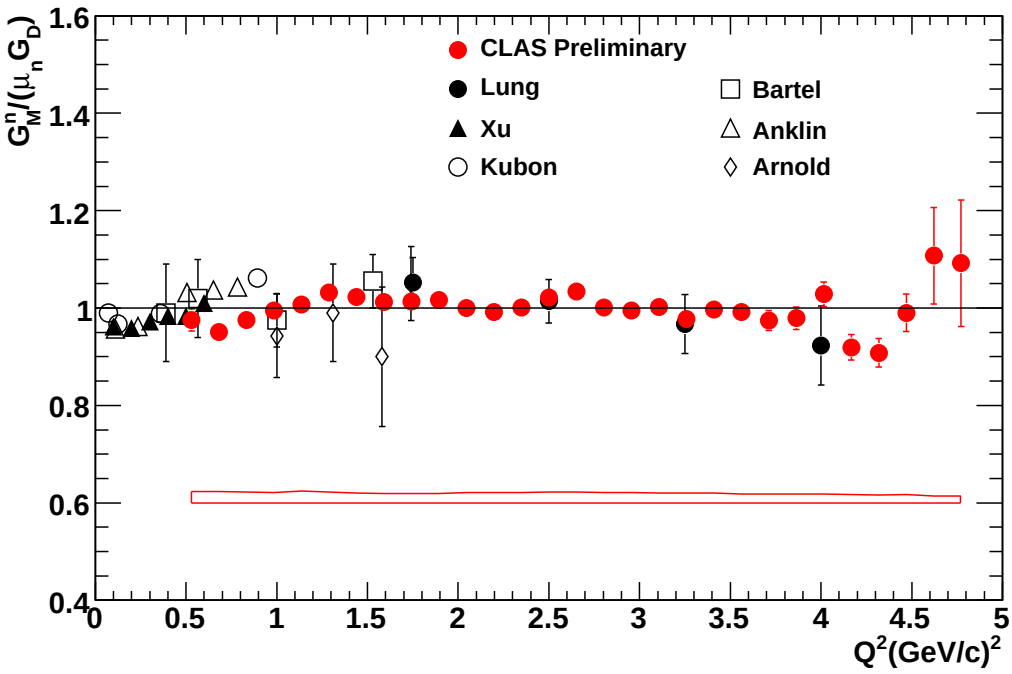

Figure 1: Selected results for the neutron magnetic form factor G_M^n in units of $\mu_n G_D$ as a function of Q^2. See Reference [3] and references therein.

Measuring G_M^n at higher Q^2 will shed light on important questions in hadronic physics. At asymptotically large Q^2, the elastic nucleon form factors can be rigorously calculated in perturbative QCD (pQCD) where the small wavelength of the virtual photon ensures that the quark substructure of the nucleon can be resolved [10]. It is assumed the nucleons can be treated as bound systems of point-like quarks governed by the properties of the strong interaction. Dimensional scaling predicts that only valence quarks will be important and those quarks interact via a hard-scattering process. These calculations reproduce the Q^2 dependence of the proton magnetic form factor for $Q^2 > 10$ GeV^2. The transition from the low-Q^2 dipole form to the pQCD regime is still unclear. Evidence from recent Jefferson Lab experiments and others suggest that non-perturbative effects still dominate the form factors for $Q^2 < 10$ GeV^2. For example, the Q^2 dependence of the ratio $\mu_p G_E^p/G_M^p$ is expected to be constant in pQCD, but surprising Jefferson Lab measurements of this ratio revealed significant Q^2 dependence up to $Q^2 = 5.0$ GeV^2 [11, 12, 13]. Figure 2 shows the quantity $\mu_p G_E^p/G_M^p$ measured in several experiments. The points labeled Punjabi and Gayou are the Jefferson Lab measurements and are not constant with Q^2. Higher Q^2 investigations show evidence of scaling behavior, consistent with predictions of quark dimensional scaling and

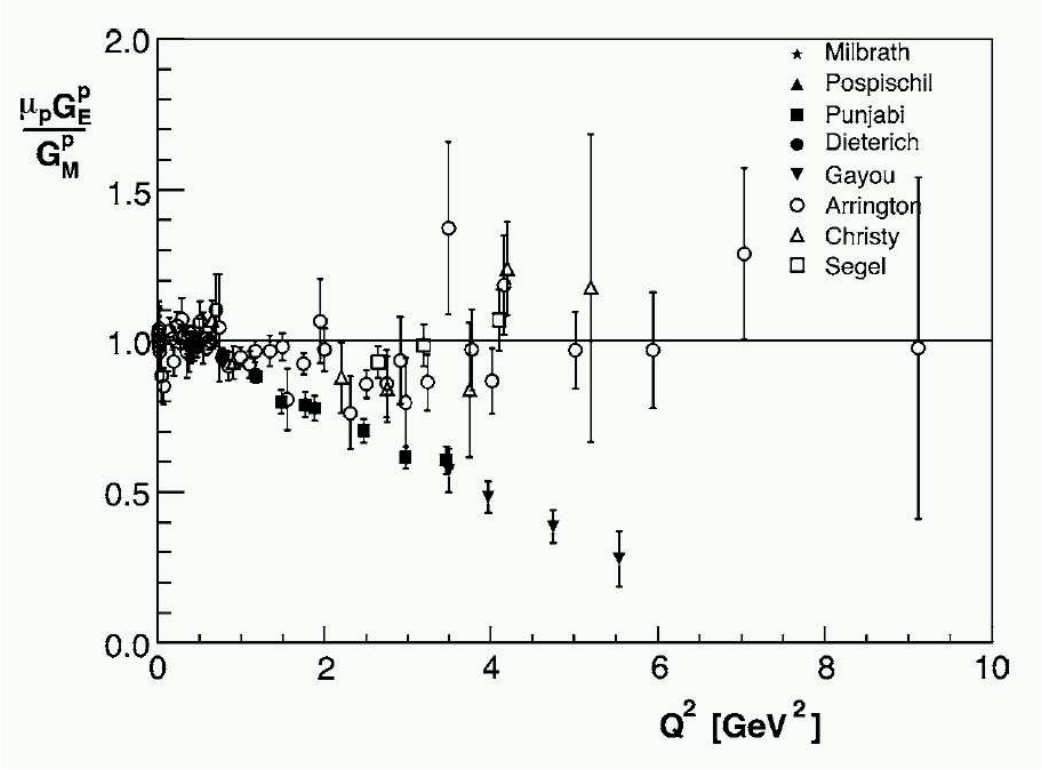

Figure 2: The ratio $\mu_p G_E^p / G_M^p$ from polarization transfer measurements, recent Rosenbluth data, and a reanalysis by Arrington of older SLAC data. See reference [2] and references therein.

perturbative QCD [11].

The elastic nucleon form factors are a fundamental challenge for lattice QCD calculations. Full calculations are still beyond our reach so existing ones use different approximations. These include techniques like the 'quenched approximation' where dynamical effects of quarks on the vacuum are ignored and the use of quark masses much higher than the physical ones (by a factor of 5-20) [14]. Extrapolations are then made to the physical quark mass region. Some success has been achieved in reproducing the Q^2 dependence of G_M^n for $Q^2 < 1.0$ GeV^2, but the higher Q^2 region remains new territory [14].

Recent theoretical work has led to the development of generalized parton distributions (GPDs) where form factors and structure functions can be simultaneously embedded. These distributions hold the promise of performing nuclear tomography and developing a three-dimensional image (two spatial and one momentum coordinate) of the nucleon. They have 'tremendous potential to provide a quantitative description of the quark motion inside hadrons' [15]. GPDs are typically studied via deeply virtual Compton scattering or real Compton scattering at high momentum transfer. However, the elastic form factors (G_M^n, G_E^n, G_M^p, and G_E^p) are key constraints on GPDs. The lowest moments of the GPDs multiplied by the appropriate quark charges and summed over all quark flavors recover the form

factors as shown below

$$G_M^n(t) = \int_{-1}^{+1} dx \sum_q \left(e_q H^q(x,\zeta;t) + \kappa e_q E^q(x,\zeta;t)\right) \tag{7}$$

where t is the invariant momentum transfer, x is the longitudinal momentum fraction, ζ is the skewness, and H^q and E^q are the flavor-dependent generalized parton distributions [16, 17]. The GPD E^q is mostly unknown. These sum rules hold for all values of Q^2 from zero to infinity. Measuring the nucleon form factors complements other proposed 12-GeV programs to measure deeply virtual exclusive (DVE) reactions at low momentum transfer $|t|$. The form factors connect to the GPDs at high $|t|$ ($= Q^2$ for elastic scattering) and so high-Q^2 data are needed to obtain the structure of the nucleon at small transverse distances [18]. A particularly interesting possibility is to extract the u- and d-quark contributions to G_M^n, but this analysis requires broad Q^2 coverage of all four elastic nucleon form factors. There are some indications that the u- and d-quark contributions behave differently at large Q^2 which may also shed light on the existence of dimensional scaling at low Q^2 [17].

We note that the effort to measure G_M^n in the range $Q^2 = 2 - 14$ GeV^2 is part of a larger Jefferson Lab program to increase our understanding of all four nucleon form factors and express them in terms of common GPDs. All four elastic form factors are needed to untangle the different quark contributions. However, at high Q^2 there is precise data only for the proton. The limited coverage can be seen by comparing Figure 1 with Figure 3 which shows the normalized proton magnetic form factor G_M^p. The G_M^p data extend out to $Q^2 = 30$ GeV^2 while the G_M^n data in Figure 1 are just now being extended to $Q^2 = 4.5$ GeV^2 (red circles in Figure 1 from Lachniet, *et al.* [3]). With the 12-GeV Upgrade of CEBAF, G_E^p/G_M^p and G_M^n can be measured up to $Q^2 \approx 14$ GeV^2 and for G_E^n up to $Q^2 = 5$ GeV^2 [18]. This nucleon form factor program will be part of a 'great leap forward in our knowledge of hadron structure' [18].

3 The Experiment

3.1 The Ratio Method

We propose to use the ratio of quasielastic $e-n$ to $e-p$ scattering from a deuterium target to measure G_M^n in the range $Q^2 = 2 - 14$ GeV^2. This technique has been shown to significantly reduce the uncertainties associated with other methods and has already been used by us [3, 4] and others [2, 5, 6, 7, 8] to measure G_M^n. See Figure 1 for the results of the E5 measurement and other data on G_M^n. The method is based on the ratio

$$R = \frac{\frac{d\sigma}{d\Omega}(D(e,e'n))}{\frac{d\sigma}{d\Omega}(D(e,e'p))} \tag{8}$$

for quasielastic kinematics. It is nearly equal to the ratio of the free nucleon $e-n$ to $e-p$ cross sections. In terms of the free nucleon form factors

$$R = a(Q^2)\frac{\sigma_{mott}^n(G_E^{n\,2} + \frac{\tau_n}{\varepsilon_n}G_M^{n\,2})\left(\frac{1}{1+\tau_n}\right)}{\sigma_{mott}^p(G_E^{p\,2} + \frac{\tau_p}{\varepsilon_p}G_M^{p\,2})\left(\frac{1}{1+\tau_p}\right)} \quad . \tag{9}$$

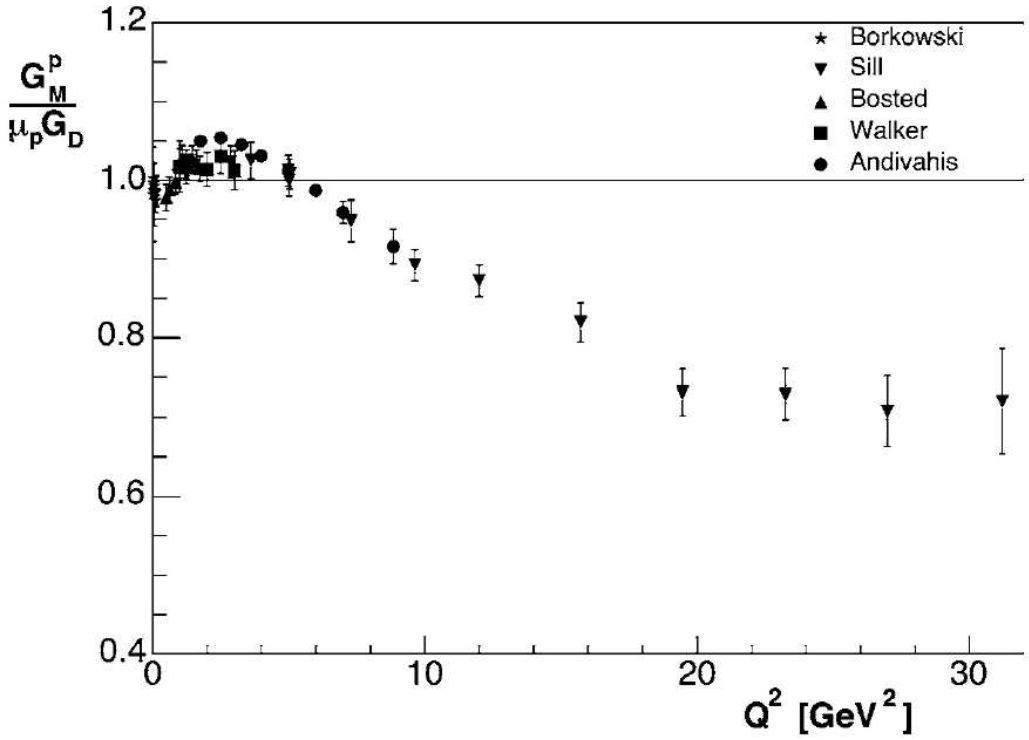

Figure 3: World data for proton magnetic form factor G_M^p, in units of $\mu_p G_D$, as a function of Q^2. See [2] and references therein. Compare with Figure 1.

Deviations from this 'free ratio' assumption are parametrized by the factor $a(Q^2)$ which can be calculated from deuteron models and is close to unity at large Q^2. Once the model corrections have been applied to R, the results of other measurements of the proton form factors (see Figures 2 and 3) and the neutron electric form factor (see Figure 4) can be used to extract G_M^n. The neutron electric form factor shown in Figure 4 is smaller than G_M^n by a factor of six or more and its contribution is kinematically suppressed at large Q^2 so it has little effect on extracting G_M^n in this way.

The ratio method has several advantages. It is insensitive to the luminosity, electron acceptance, electron reconstruction efficiency, trigger efficiency, the deuteron wave function, and radiative corrections. The price one pays is the technique requires a precise measurement of the neutron detection efficiency and careful matching of the neutron and proton acceptances. The experiment performed in CLAS in the E5 run period used a unique dual-cell target, containing collinear deuterium and hydrogen cells to make *in-situ* calibration measurements simultaneously with data collection on deuterium. We plan to follow a similar path at higher Q^2. Below we discuss more details on the challenges posed by this measurement.

3.2 Quasielastic Event Selection

The ratio method described above relies on the selection of quasielastic $e-n$ and $e-p$ scattering. In the previous CLAS measurement of G_M^n a cut on θ_{pq}, the angle between the

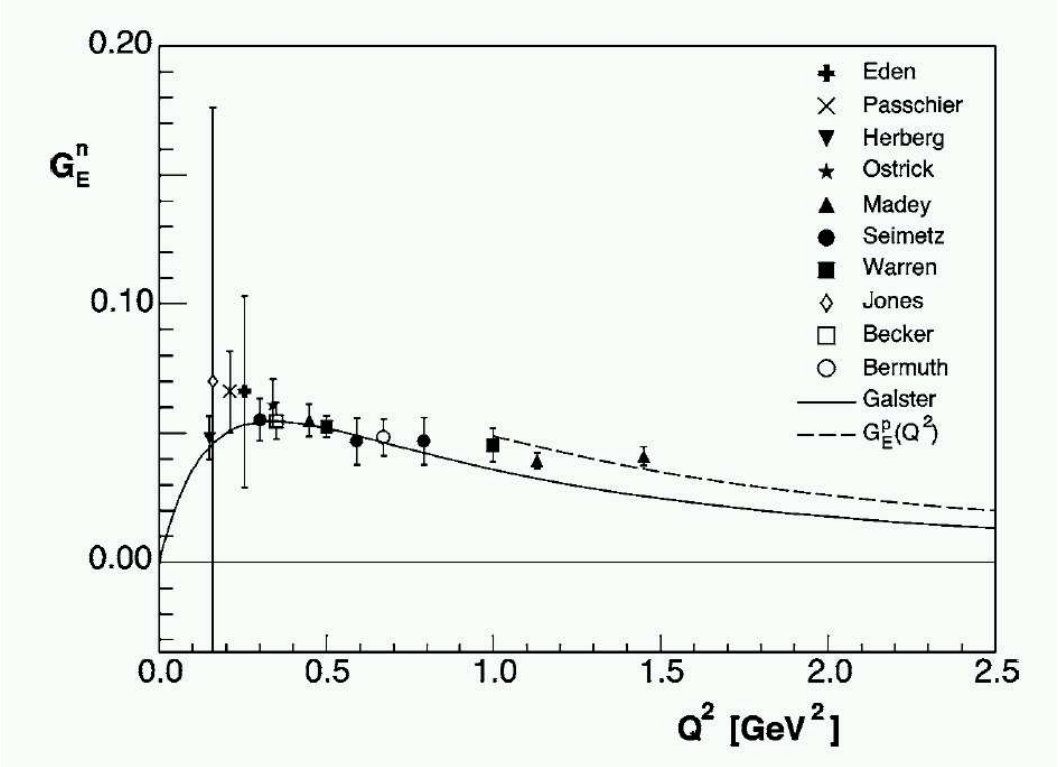

Figure 4: The neutron electric form factor G_E^n as a function of Q^2. See [2] and references therein. Results from ^{3}He are indicated by open symbols. The full curve shows the Galster [9] parameterization; the dashed curve represents the Q^2-behavior of G_E^p.

ejected nucleon and the virtual photon, was used to select these events. See Figure 5 for definitions of the relevant angles. This angle cut θ_{pq}^{max} was varied with Q^2 and an additional cut on W^2 ($0.5 \leq W^2 \leq 1.2$ $(GeV/c^2)^2$) was required. Figure 6 shows the effectiveness of the θ_{pq}^{max} cut on reducing the inelastic background for the previous CLAS measurement of G_M^n. At higher energy and momentum transfer we expect quasi-free kinematic effects to broaden the W^2 distribution and focus the θ_{pq} distribution more tightly along the virtual photon direction. We have developed a simulation to test the effectiveness of this method in selecting quasielastic events. In Section 3.2.1 we discuss the simulation we have developed and study the effectiveness of the θ_{pq}^{max} cut and other strategies in Section 3.2.2-3.2.3.

3.2.1 Monte Carlo Simulation of $D(e,e'p)n$ and $D(e,e'n)p$

To simulate the quasielastic production we treat the deuteron as composed of two, on-shell nucleons, one of which will act as a spectator in the interaction. The quasielastic interaction is then elastic scattering with the target nucleon, but we must also add the effect of the Fermi motion of this target nucleon within the deuteron. This approach enables us to take advantage of existing data on electron scattering on the proton and the deuteron.

We start with the existing, elastic, nucleon form factors. We use Equations 3-6 and

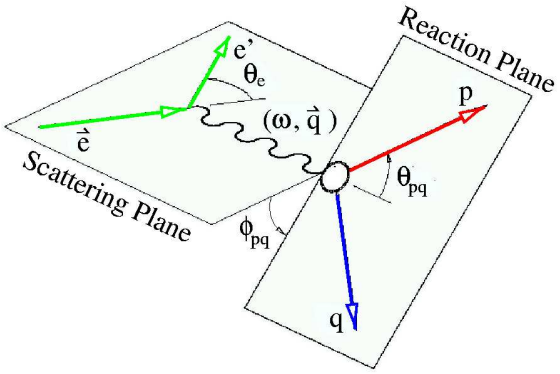

Figure 5: Kinematics of $D(e,e'p)n$ and $D(e,e'n)p$.

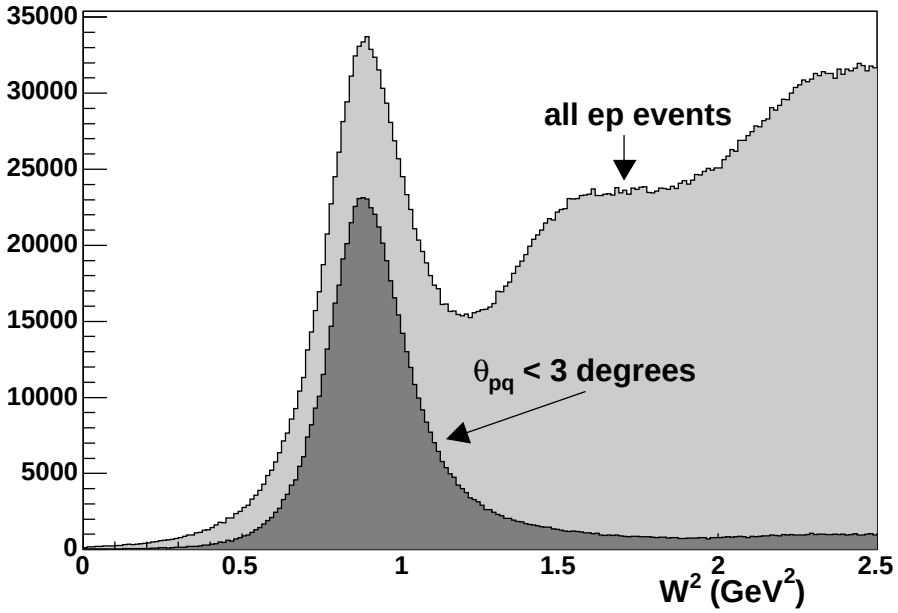

Figure 6: Effect of the cut on θ_{pq}, the angle between the direction of the virtual photon and the direction of the nucleon for the CLAS $4-$GeV, G_M^n data [3].

make the following assumptions about the form factors

$$G_E^p \approx G_D = \frac{1}{(1+Q^2/\Delta)^2} \qquad G_M^p \approx \mu_p G_D \qquad G_M^n \approx \mu_n G_D \qquad G_E^n = \frac{\mu_n \tau G_D}{1+\eta\tau} \tag{10}$$

where μ_n and μ_p are the neutron and proton magnetic moments, $\Delta = 0.71$ $(\mathrm{GeV/c})^2$, and $\eta = 5.6$ (from the Galster parameterization [9]). The number of quasielastic events in a particular Q^2 bin is calculated from these elastic form factors. Next, the Fermi momentum $\vec{p}_f$ for one of the nucleons is chosen at random (the spectator nucleon has momentum $-\vec{p}_f$)

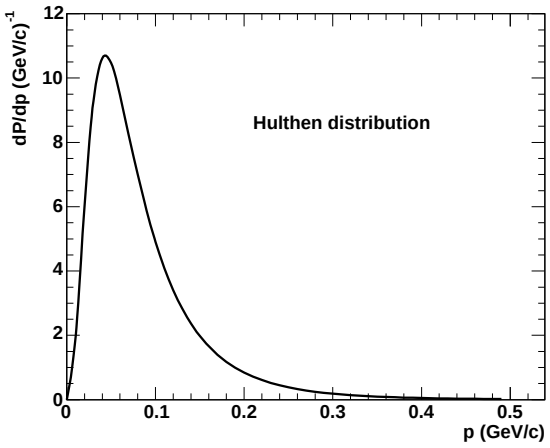

Figure 7: Hulthen distribution representing the nucleon Fermi momentum inside the deuteron.

and we simulate the kinetics of the scattering. The nucleon momentum $\vec{p}_f$ inside the deuteron is chosen from the Hulthen distribution shown in Figure 7 and depends only on the p_f [24].

We also have to account for combined effect of the Fermi motion and the beam energy dependence of the elastic cross section. A nucleon whose Fermi motion is directed towards the incoming electron will observe a higher energy beam in its rest frame and (because of the elastic cross section dependence on the beam energy) will have a lower cross section for interacting. Conversely, a nucleon 'running away' from the beam will see a lower effective beam energy and have a higher cross section.

We now describe a way to account for this effective-beam-energy effect and the momentum distribution of the target nucleon. We start with the quasielastic case. For a given choice of Fermi momentum p_f and nucleon polar angle $\cos\theta$ there is an effective beam energy in the rest frame of the moving nucleon. The angle θ here is the angle between the direction of the moving target nucleon and the beam axis in the laboratory. The size of the cross section at this effective beam energy in the nucleon rest frame and the Hulthen distribution will determine the relative weight of this $p_f - \cos\theta$ combination. At each effective beam energy in the quasielastic case the Brash parameterization [25] of the nucleon cross section is used to obtain the cross section dependence on the electron scattering angle. This angular dependence is integrated over the CLAS12 angular acceptance to obtain the weighting due to the effective-beam-energy effect at each $p_f - \cos\theta$ point. Multiplying this effective-beam-energy weight with the Hulthen distribution at each $p_f - \cos\theta$ point yields the weight functions for electron-proton and electron-neutron scattering. The results are shown in Figure 8. The Hulthen distribution produces a long ridge in the range of the Fermi momentum $p_f \approx 0.04 - 0.05\ GeV/c$ and the cross section dependence on the effective beam energy creates a downward slope along this ridge from forward to backward angles. We can now use these functions to choose the the Fermi momentum $\vec{p}_f$ for the quasielastic case.

The algorithm for simulating the Fermi motion is as follows. (1) Choose the value of

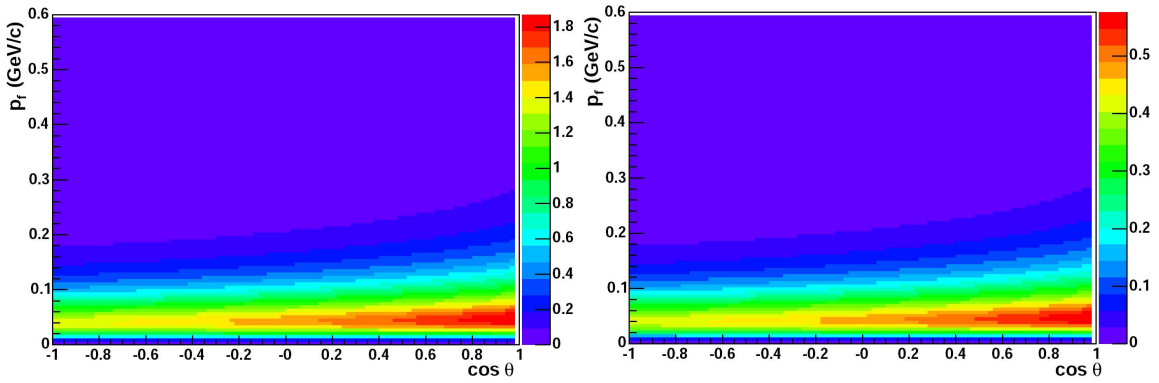

Figure 8: Plot of the weighting function for electron-proton (left-hand panel) and electron-neutron (right-hand panel) scattering. The beam energy is 11 GeV. The angle θ is the angle between the direction of the moving target nucleon and the beam axis in the laboratory.

Q^2 and the type of nucleon. The Q^2 dependence of the elastic form factors for both neutrons and protons is used as the weighting function for this step. (2) Next, the magnitude of the Fermi momentum p_f and $\cos\theta$ are picked from the distributions in Figure 8. The azimuthal angle ϕ_f of the nucleon is chosen from a uniform, random distribution in the range $\phi_f = 0 - 2\pi$. (3) Once the Fermi momentum is chosen, a relativistic boost is made to the rest frame of the nucleon for all particles and the coordinate system is rotated so the incoming electron is along the z axis. A new beam energy is calculated. (4) A nucleon, rest-frame electron scattering angle is chosen from a random distribution weighted by the Brash parameterization. (5) Last, the momenta of the electron and nucleon are transformed back to the laboratory frame. A method like this one was implemented in the program QUEEG and used to simulate quasielastic events here [3].

We have also calculated the contribution of the inelastic channels because it will form a background under the quasielastic peak. We again treated the deuteron in the spectator approximation as two, on-shell nucleons described by the Hulthen distribution. To determine the weighting function for each $p_f - \cos\theta$ point we use the Hulthen distribution as before, but there is no set of formulas for the inelastic cross section comparable to the elastic form factors. To calculate the inelastic cross section at a particular value of Q^2 and account for the effective-beam-energy effect in the entrance channel we have to estimate the inelastic cross section for the $p(e,e')X$ reaction near the quasielastic peak. We use inclusive measurements of the inelastic cross section on the proton from Reference [26] and shown in Figure 9. These inelastic, inclusive electron spectra cover the full range of Q^2 of CLAS12. For the neutron case we used measurements of inclusive electron scattering on deuterium where the ratios of $n - p$ cross sections were extracted [28]. These measurements are shown in Figure 10. The measurements on deuterium do not cover the full Q^2 range of CLAS12, but the ratios of neutron to proton cross section in the scattering from deuterium are roughly constant up to $Q^2 = 8$ (GeV/c)^2. We extrapolate these ratios to cover the CLAS12 Q^2 range. To generate the inelastic weighting function an effective beam energy for each $p_f - \cos\theta$ pair is calculated. The inelastic cross section is integrated over the CLAS12 angular range and

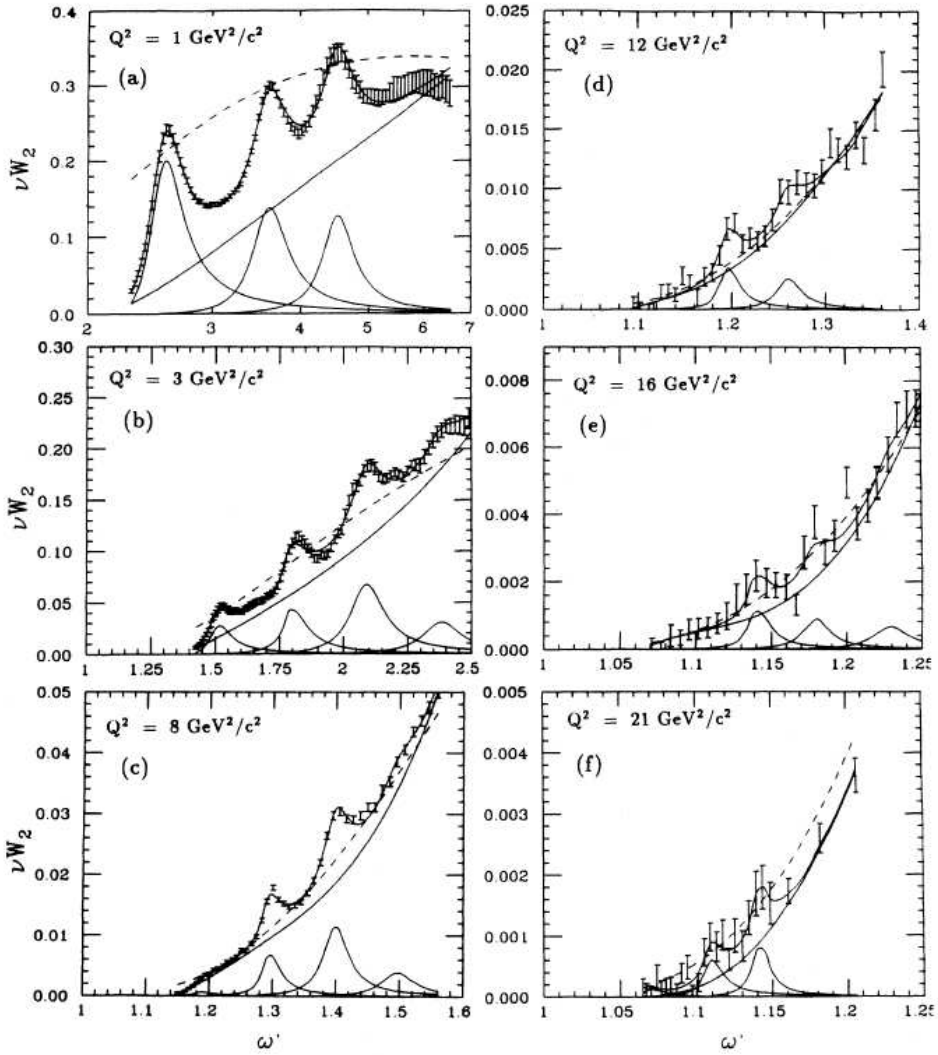

Figure 9: The structure functions νW_2 versus ω' for inclusive inelastic scattering in the resonance region for various values of nominal Q^2, where $\omega' = 1 + W^2/Q^2$. The experimental data were obtained from Reference [26] and references therein. The solid curves are resonant fits to the data. The dashed curves are fits to the data in the scaling region extrapolated down to the resonance region as a test of duality .

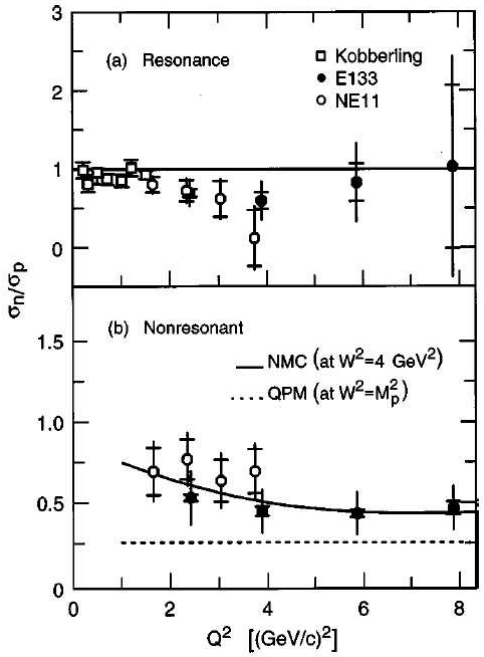

Figure 10: The ratios (a) $(\sigma_n/\sigma_p)_\Delta$ and (b) $(\sigma_n/\sigma_p)_{nonres}$ for inelastic electron scattering from deuterium from Reference [28].

over the range $W^2 = 0.0 - 3.0\ (GeV/c^2)^2$. The upper limit on the W^2 integration is chosen large enough to include high-W^2 events that might be smeared by the kinematics into the quasielastic peak. Multiplying the Hulthen distribution by this effective-beam-energy weight gives the final weighting function for picking p_f and $\cos\theta$. The result is shown in Figure 11 Note the similarity with the distributions in Figure 8.

To simulate the inelastic part we now follow a procedure analogous to what was done in the quasielastic case. (1) The number of inelastic events in a Q^2 bin is estimated by interpolating the cross section between the measured inelastic cross sections shown in Figure 9 for quasielastic scattering off the proton and combined with the ratios in Reference [28] for quasielastic scattering off the neutron. (2) The Fermi momentum (p_f and $\cos\theta$) are chosen from the distribution in Figure 11. The azimuthal angle ϕ is chosen from a uniform, random distribution over the range $\phi = 0 - 2\pi$. (3) A relativistic boost is then made to the rest frame of the moving nucleon and the effective beam energy calculated. (4) At this point final, inelastic state ($e' - p - \pi^0$, $e' - n - \pi^+$, ...) needs to chosen and the decay of short-lived particles and final 4-vectors performed. To do this task we use a modified version of the program genev from the Genova group [32]. This code includes a wide range of inelastic exit channels for $e - p$ and $e - n$ scattering and the Q^2 dependence follows a dipole form for this inelastic component that is similar to what has been observed [27]. This Monte Carlo code produces the final inelastic state using the effective beam energy as input. (5) The 4-vectors of final particles are then transformed from the nucleon rest frame back to the laboratory frame. We have modified the original genev program (and called it genevD) to include the Fermi motion and use the Jetset libraries [33] to perform the relativistic transformations.

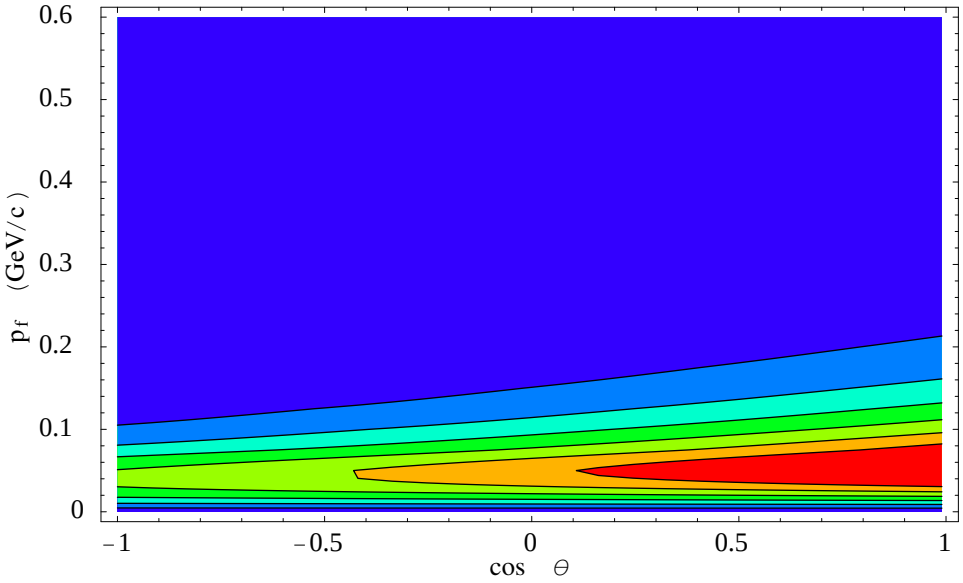

Figure 11: Weighting function of the inelastic cross section for protons. The beam energy is 11 GeV. The angle θ is the angle between the direction of the moving target nucleon and the beam axis in the laboratory.

To summarize, we use the Brash parameterization of the elastic cross section to choose the number of quasielastic events in a particular Q^2. For the inelastic cross section we interpolate between the measured inclusive cross section. The Fermi momentum in each case is chosen with the combined weights of the Hulthen distribution and the cross section dependence on the effective beam energy at each $p_f - \cos\theta$ point. Once the Fermi momentum is determined, the system is boosted to the nucleon rest frame. The final 4-vectors are chosen from the Brash parameterization (quasielastic case) or with the genevD program (inelastic case). The final states are then transformed back to the laboratory frame.

After the 4-vectors have been generated the next step is to filter these thrown events with the code FASTMC [35]. This program contains a parameterization of the CLAS12 acceptance and the anticipated resolutions. Each event is tested to see if it lies in the CLAS12 acceptance and the final momentum and position are smeared with the resolutions. In the last stage of the simulation the ROOT program from CERN is used for final analysis and presentation.

3.2.2 Kinematic cuts for Quasielastic $D(e, e'p)n$

We now demonstrate our ability to identify quasielastic events in the $D(e, e'p)n$ reaction with CLAS12. In Figure 12 the acceptance for quasielastic $D(e, e'p)n$ reaction is shown for a beam energy of 11 GeV and for the full range of Q^2. For charged particles, the forward tracking system covers the range $\theta = 5^\circ - 40^\circ$ with a system consisting of a silicon vertex tracker, drift chambers, Cerenkov counters, TOF scintillators, and electromagnetic calorimeters. For larger angles ($40^\circ - 135^\circ$) there is a central tracker consisting of layers of silicon (or possibly micromegas), TOF scintillators, and calorimeters. The acceptance is

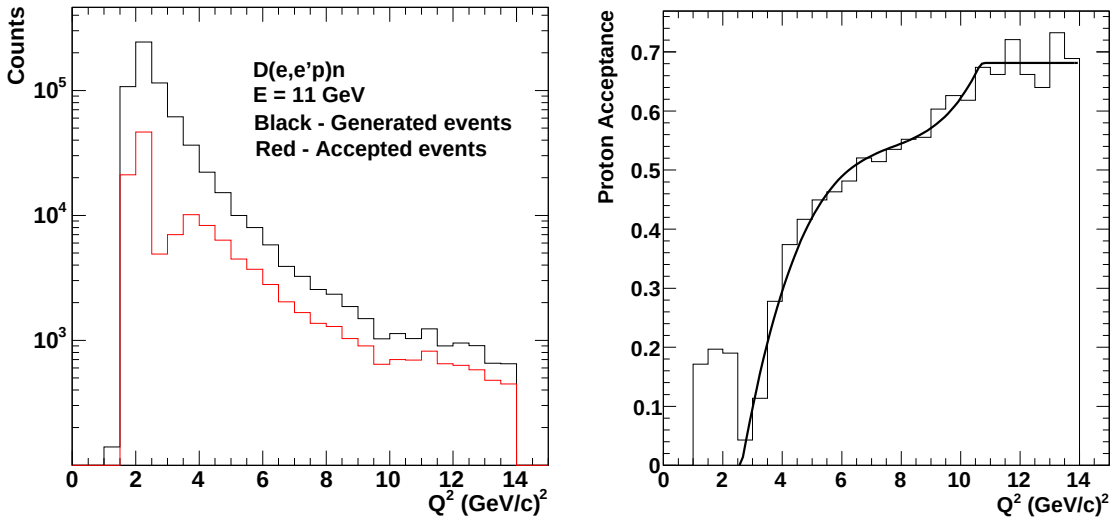

Figure 12: Acceptance for the $D(e,e'p)n$ reaction in CLAS12 at 11 GeV. The left-hand panel shows the number of events as a function of Q^2 for generated and accepted events in our simulation. The right-hand panel shows the acceptance function extracted from those distributions. We neglect the peak in the acceptance at low Q^2 in our fit because we focus here on the forward detector and that low-Q^2 peak in the acceptance is due to the central detector in CLAS12.

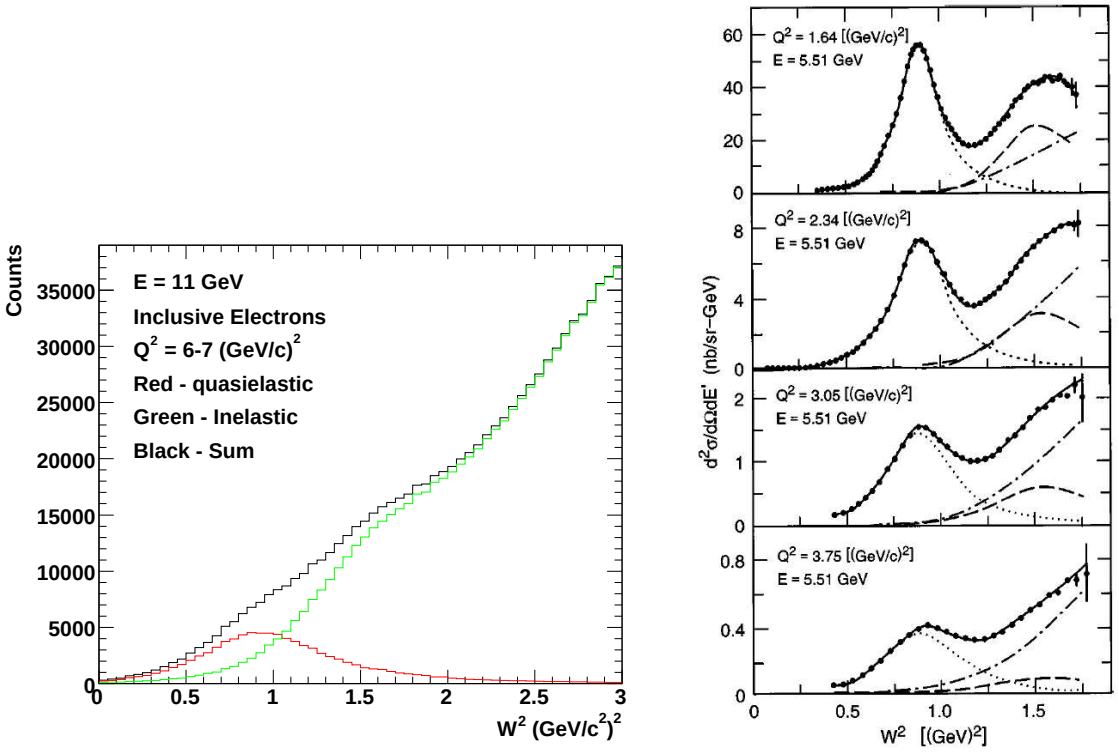

Figure 13: Comparison of the W^2 spectra for simulated inclusive electrons (left-hand panel) from this work and measured inclusive spectra for electron scattering on deuterium from Reference [28] (right-hand panel). Inelastic $e-d$ cross sections are shown in the $\Delta(1232)$ resonance region fitted with contributions from quasielastic (dotted line), $\Delta(1232)$ (dashed), and non-resonant (dot-dashed) contributions.

small at low Q^2 corresponding to forward angles where the CLAS12 torus coils are converging. At larger angles (and Q^2) the acceptance increases to about 70%. To study our ability to separate quasielastic from inelastic events we focus on the range $Q^2 = 6-7$ (GeV/c2)^2; in the middle of the available Q^2 range shown in Figure 12. In the previous measurement of G_M^n with CLAS, a cut on the angle between the ejected nucleon and the virtual photon θ_{pq} was used to select quasielastic events from a sample of $e-p$ and $e-n$ coincidences. An additional cut $W^2 \leq 1.2$ $(GeV/c^2)^2$ reduced the contribution of the inelastic cross section to the quasielastic peak. We explore the same method here.

Starting with Figure 13, we show in the left-hand panel the W^2 spectrum for inclusive electrons for a beam energy of 11 GeV and $Q^2 = 6-7$ (GeV/c)^2. The red histogram is from quasielastic events, the green is the inelastic contribution, and the black histogram is the sum of the two. Note the large width of the quasielastic peak of about 0.7 $(GeV/c^2)^2$. At this Q^2 range the inelastic contribution is much larger than the quasielastic one, consistent with previous observations one of which is shown in the right-hand panel. These are data from Reference [28] at a similar Q^2 range but a higher beam energy (15.74 GeV versus 11 GeV in our calculation). The quasielastic peak is just visible as a shoulder on a broad peak. These

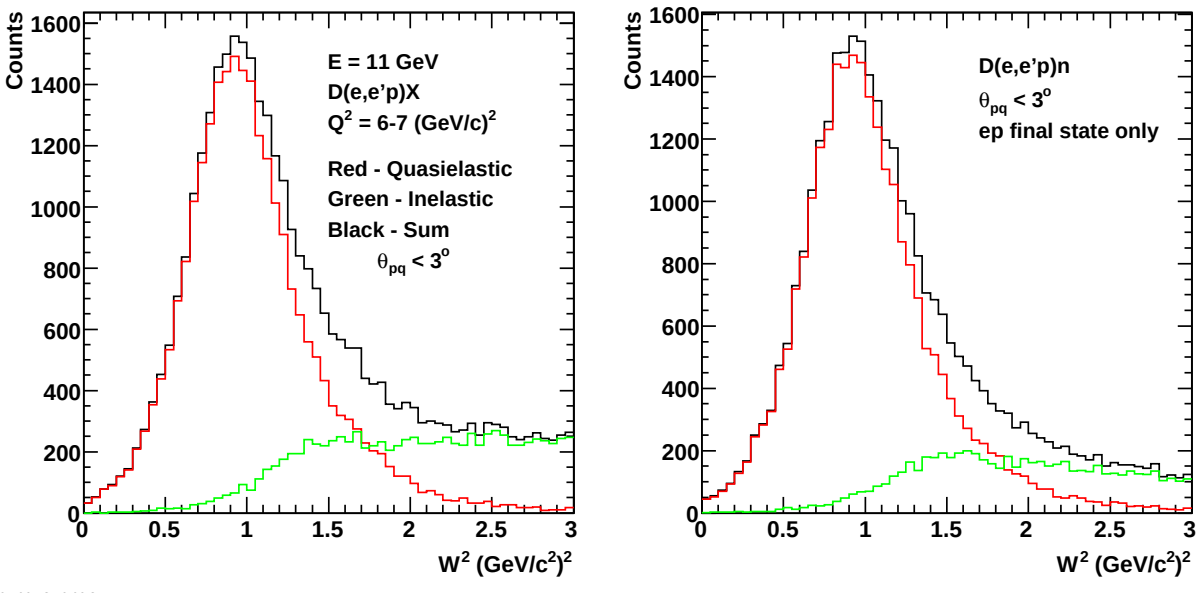

Figure 14: W^2 spectra for $D(e,e'p)X$ (left-hand panel) and with only an electron and proton in the final state (right-hand panel). Both spectra are for $\theta_{pq} < 3°$.

plots emphasize the challenge we face in selecting the quasielastic events in our data.

The left-hand panel in Figure 14 shows the W^2 spectra for the reaction $D(e,e'p)X$ with the additional requirement that $\theta_{pq} \leq 3°$. We will discuss the reasoning behind this value of the limit on θ_{pq} below. The inelastic background has been greatly suppressed and the quasielastic peak (in red) is now clearly visible. The inelastic part contributes about 5% in the region $W^2 \leq 1.2$ $(GeV/c^2)^2$. We have also explored another cut on the data set to reduce the inelastic background further. With the greater hermiticity of CLAS12 (compared to CLAS) and the higher multiplicity of events at these beam energies, it is likely that we will capture a large fraction of the three- and four-particle final states produced in CLAS12. Reactions that produce, say, Δ^+ particles in the final state which then decay to $p\pi^0$ (with the subsequent decay $\pi^0 \rightarrow 2\gamma$) can mimic the quasielastic events we desire, but if we can detect one of the additional particles we can use that information to reduce the inelastic background. In the right-hand panel of Figure 14 we have added this additional requirement that only an electron and proton be detected in the final state and nothing else. There is some limited reduction in the inelastic background. The fraction of inelastic events contaminating the quasielastic peak drops from 5% to 4% in the region $W^2 < 1.2(GeV/c^2)^2$. We will return to this technique below when we consider the selection of quasielastic neutrons.

To illustrate further the effect of the θ_{pq} cut to suppress the inelastic background consider Figure 15. It displays the angular distribution of θ_{pq} for the same simulations discussed in Figures 12-14. The red histogram represents the quasielastic contribution and is more forward peaked than the inelastic (green) contribution. The large inelastic background (recall Figure 13) is found mostly at higher θ_{pq} where we can use kinematic cuts to eliminate much

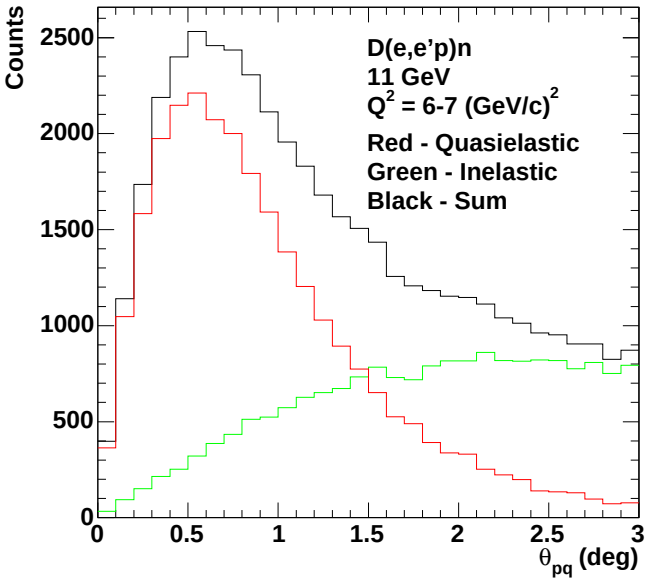

Figure 15: Distribution of θ_{pq} for the simulations discussed in Figures 12-14.

of it. We set the cut at $\theta_{pq} = 3^\circ$ to capture most of the quasielastic events.

Finally, we consider the angular resolution of CLAS12. Figure 16 shows the dependence of the angular resolution $\Delta\theta$ in CLAS12 for charged particles on particle momentum [29]. The angle of the track relative to the beam at the vertex was 35°. Calculations with other initial angles produce very similar curves. The design specification is 0.5 mrad (the dashed line) which the detector will meet over much of the momentum range. The increase in $\Delta\theta$ at low momentum is due primarily to multiple scattering. This resolution is more than adequate to precisely measure the θ_{pq} angular distribution. We performed a test by arbitrarily increasing the size of $\Delta\theta$ by 50% in our simulation and found no change in the angular distributions shown in Figure 15.

3.2.3 Kinematic cuts for Quasielastic $D(e, e'n)p$

We now discuss our ability to separate quasielastic events in the $D(e, e'n)p$ reaction from the inelastic background in CLAS12. In Figure 17 the acceptance for the $D(e, e'n)p$ is shown for a beam energy of 11 GeV and the full Q^2 range. For neutrons, the forward detection system consists of TOF scintillators and electromagnetic calorimeters and covers the angular range $5^\circ - 40^\circ$. In this discussion we focus on the calorimeters because they have much higher efficiency and will be the primary neutron detector. We found in the CLAS measurement of G_M^n that the TOF scintillators provided a useful consistency check on our analysis. In Figure 17 the acceptance vanishes at small Q^2 (and forward electron angles) where the torus coils are converging along the beam pipe and it increases to about 30-40% at high Q^2 and large electron angles. The neutron simulation includes the effect of

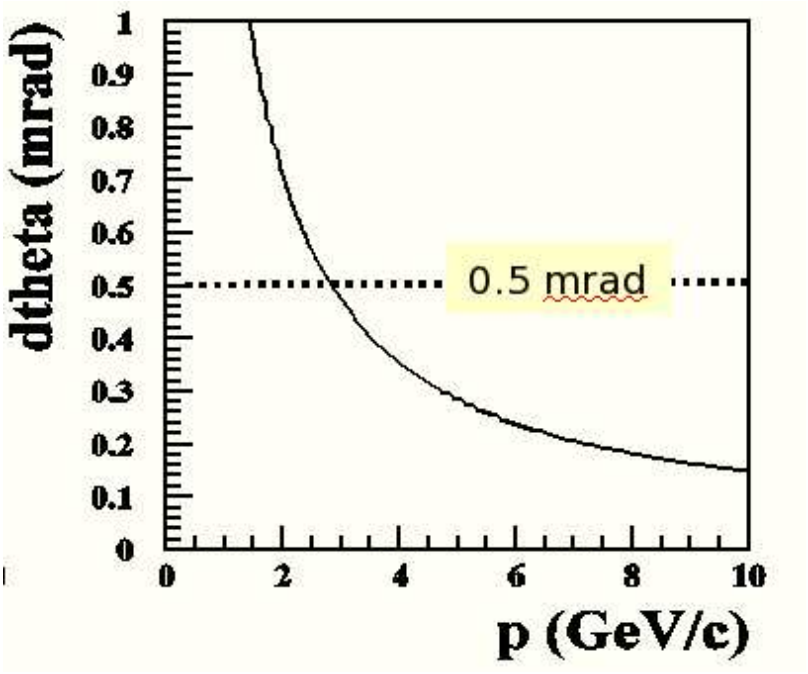

Figure 16: Angular resolution of CLAS12 for charged particles in the forward tracking system.

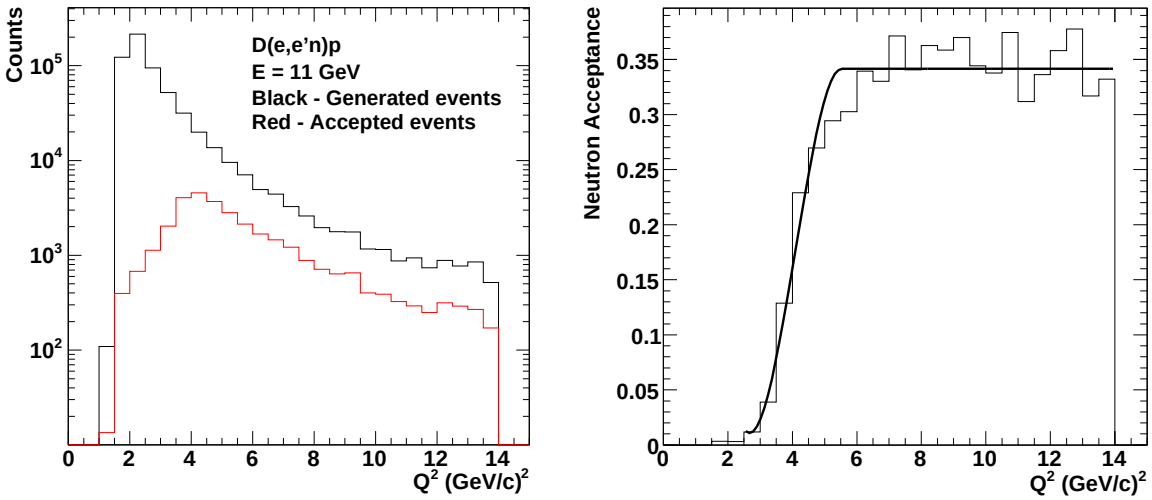

Figure 17: Acceptance for the $D(e, e'n)p$ reaction at 11 GeV. The left-hand panel shows the number of events as a function of Q^2 for generated and accepted events in our simulation. The right-hand panel shows the acceptance function extracted from those distributions.

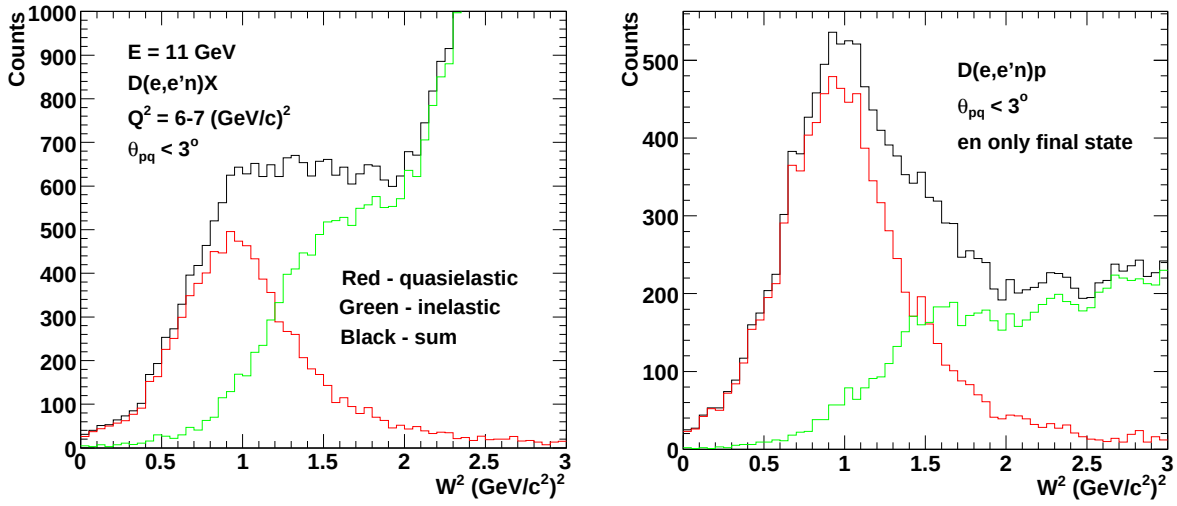

Figure 18: Comparison of the simulated W^2 spectra for the $D(e,e'n)X$ (left-hand panel) and $D(e,e'n)p$ reactions (right-hand panel). Both spectra are for $\theta_{pq} < 3°$.

the neutron detection efficiency which reaches a maximum of 60% in the simulation. The maximum value is based on our experience with the CLAS G_M^n measurement and the results of a recent simulation of CLAS12 using GSIM12 [30]. As before we focus on the middle of this 4-momentum transfer range ($Q^2 = 6-7$ (GeV/c)^2) and use the same cut on θ_{pq} to select quasielastic events along with the restriction that $W^2 \leq 1.2$ $(GeV/c^2)^2$. We note here that in this proposal and in the analysis of the CLAS G_M^n measurement, we have tried to treat the proton and neutron identically to reduce any bias in the ratio. The results of our simulation of $D(e,e'n)p$ are shown in the left-hand panel of Figure 18 for quasielastic events (red histogram), inelastic events (green histogram), and the total (black histogram). There is considerably more inelastic background here than in the proton case. This can be understood with Figure 19 which shows the θ_{pq} distribution for neutrons from our simulation. The peak in the angular distribution for neutrons is at an angle about $0.2° - 0.3°$ larger compared to the proton θ_{pq} distribution (Figure 15). The angular distribution of generated, quasielastic neutrons is similar to the one for protons which both have widths of $\approx 0.5°$. The angular resolution for protons is better (recall Figure 16), but the expected neutron angular resolution is about the same as the width of the neutron angular distribution which is adequate for this measurement. The results of a study with GSIM12 of the neutron angular resolution are shown in Figure 20. The study was performed for neutrons in the momentum range $p_n = 1-7$ GeV/c, angle ranges $\theta_n = 20° - 25°$ and $\phi_n = -3° - 3°$. The blue points in Figure 20 are for neutrons detected using the inner and outer calorimeters only and the red points show the improvement obtained when the preshower calorimeter of CLAS12 is added. This new detector has finer segmentation than the older ones which improves the resolution. The resolution lies in the range $\sigma_{\theta_n} = 0.55° - 0.65°$.

The other feature of Figure 19 is the relative strength of the inelastic contribution calcu-

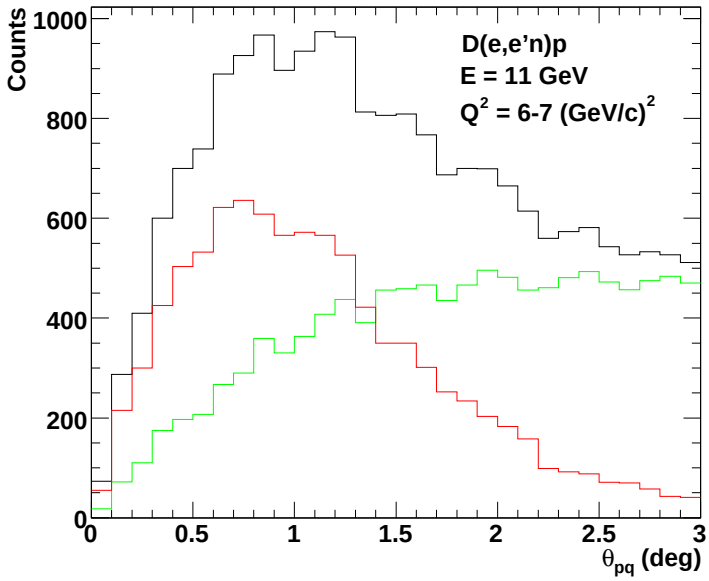

Figure 19: Angular distribution of θ_{pq} for the quasielastic (red), inelastic (green), and total (black) contributions.

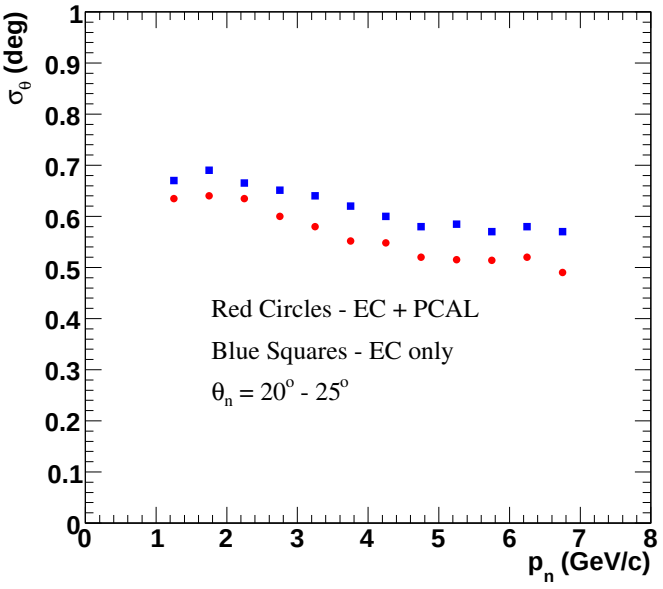

Figure 20: Angular resolution of CLAS12 for neutrons in the forward tracking system calculated with GSIM12.

lated with genevD is larger. To suppress the inelastic background we invoke the requirement that there be no more than two particles detected in the final state; the scattered electron and neutron. As discussed above, we are taking advantage of the increased hermiticity of CLAS12 to detect the additional products of inelastic reactions and use this information to veto those events. The result of applying this additional constraint is shown in the right-hand panel of Figure 18. The inelastic background is significantly reduced. For the region within our W^2 cut ($W^2 \leq 1.2$ $(GeV/c^2)^2$) the contribution of the inelastic component drops from 21% to 9% between the left- and right-hand panels.

The inelastic contributions to the proton (4%) and neutron (9%) quasielastic event sample are significant. However, in the ratio of $e-n$ to $e-p$ events this difference will be about 5% which in G_M^n will contribute about 3% which is more than we can tolerate to achieve a total precision of 3%. We can reduce this background by optimizing the choice of the maximum value of θ_{pq}, θ_{pq}^{max}, for the neutron and proton channels. Recalling Figures 20 and 16, reducing θ_{pq}^{max} will eliminate more of the background events than the quasielastic contribution down to an angle of about of $\approx 1.4^\circ - 1.5^\circ$ for both neutrons and protons. In the CLAS G_M^n measurement we used theoretical calculations to understand how different choices of θ_{pq}^{max} effected the ratio R. We can also perform careful simulations of the background and subtract it from the spectrum. The wide acceptance of CLAS12 gives us the opportunity to do this calculation effectively by using the results from the $D(e,e')X$ and $D(e,e'n)X$ reactions to calibrate the simulations. The simulations can also be tested by investigating the evolution of the spectra as θ_{pq}^{max} is varied in the data and also by adding further constraints like missing mass on the $D(e,e'p)X$ to isolate the $e-p-n$ final state for study.

3.3 Calibrations

3.3.1 Dual Target

We propose to use a collinear, dual-cell target containing deuterium (for the primary measurement) and hydrogen (for calibrations). A requirement for the ratio method described above to be successful is an accurate measurement of the neutron detection efficiency. As we will describe in more detail below this is done using the $p(e,e'\pi^+)n$ reaction. The dual-cell target will enable us to take calibration data at the same time we are collecting data for the primary measurement. This method has two important advantages. First, we will collect high-statistics, calibration data across a wide neutron momentum range. Second, the calibration data will be subject to the same running conditions as the primary measurement. Any variation in the attributes of the electron beam or CLAS12 (*e.g.* dead wires, changes in beam position on target, voltage shifts, ...) will effect both the hydrogen calibration data and the primary measurement.

This measurement will be done with the base equipment for CLAS12. The dual-cell target will be similar in design to the one used for the CLAS measurement of G_M^n during the E5 running period [31]. A conceptual drawing of the target is shown in Figure 21. Each of the cells containing liquid will be 2.0 cm in length with a 1.0 cm gap in between. The length of the cells is designed to fit within the current design of the CLAS12 silicon vertex tracker. To measure effects due to different target positions, we will collect data with the targets in opposite cells from the configuration shown in Figure 21.

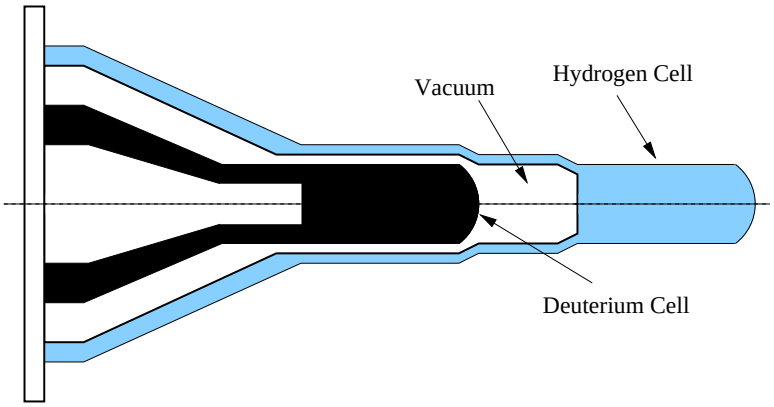

Figure 21: Conceptual design of the dual-target cell to measure G_M^n.

3.3.2 Neutron Detection Efficiency

A precise knowledge of the neutron detection efficiency is essential to keep the uncertainties of the ratio method under control. The reaction $ep \rightarrow e'\pi^+ n$ on the hydrogen part of the dual-cell target in CLAS12 will provide a source of tagged neutrons that can be used to measure the neutron detection efficiency simultaneously with the data collection on deuterium. First, the electron and positive pion will be identified. Neutron candidates will be identified using a missing mass cut ($ep \rightarrow e'\pi^+ X$) and the direction of the neutron will be inferred from the missing momentum of the $ep \rightarrow e'\pi^+(n)$ reaction. A ray will be drawn from the $e'-\pi^+$ vertex in the direction of the missing momentum to the face of the electromagnetic calorimeter (EC). If the intersection of this ray and the EC is outside of the fiducial region of the EC, the event will be dropped. If the event is inside the EC fiducial region it is classified as a reconstructed event. If the same event is found to have an EC neutron hit in the region of the intersection, then the event is counted as a found event. The neutron detection efficiency is the ratio of found to reconstructed events. These events will also be subject to other cuts to reduce background, improve particle identification, *etc.*

A second overlapping measurement of the neutron detection efficiency can be made using the time-of-flight (TOF) system in CLAS12. The same calibration reaction ($ep \rightarrow e'\pi^+ n$) will be used and a similar procedure followed to reconstruct a neutron event, except the event is required to produce a signal in one of the TOF paddles. As before, the efficiency is the ratio of found events to reconstructed ones. Other cuts will be used to reduce background events which likely will be higher in the TOF system than in the EC. For example, we found in the CLAS G_M^n analysis that requiring a minimum amount of energy deposited in the TOF reduced the photon background. This second measurement of the neutron efficiency will provide a useful cross check on the analysis.

Our studies suggest there will be adequate statistics for the neutron efficiency measurement. The requirement here is to obtain an adequate number of calibration neutrons produced by the $p(e, e'\pi^+)n$ reaction on the hydrogen part of the dual-cell target. These calibration neutrons should cover the same neutron momentum and angle range (as much as possible) as the quasielastic, $e - n$ events from deuterium. The CLAS12 acceptance for the

$D(e,e'n)p$ reaction in quasielastic kinematics is shown in Figure 22. The neutron production

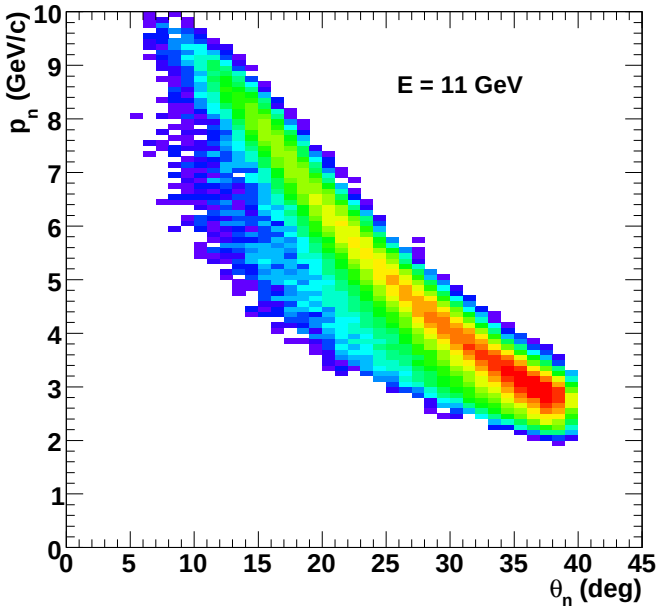

Figure 22: Neutron acceptance for the $D(e,e'n)p$ reaction in quasielastic kinematics.

extends from low-Q^2 (low p_n and high θ_n) to high Q^2 where the neutron momentum is high ($p_n \approx 9\ GeV$) and angle is forward ($\theta_n \approx 7^\circ$). The cross section for the $p(e,e'\pi^+)n$ reaction is not well known across the Q^2 range that will be accessible with CLAS12.

To study this question, we have modeled the Q^2 behavior of the π^+ production in CLAS12. The coincidence cross section for meson electroproduction in the one-photon exchange approximation can be written as [34]

$$\frac{d^3\sigma}{d\Omega dE' d\Omega_\pi} = \Gamma_V \frac{d\sigma_V}{d\Omega_\pi} \tag{11}$$

where the virtual photon flux factor Γ_V is

$$\Gamma_V = \frac{\alpha}{2\pi^2}\frac{E'}{E}\frac{K}{Q^2}\frac{1}{1-\epsilon} \tag{12}$$

and

$$K = \frac{W^2 - Q^2}{2M} \qquad \text{and} \qquad \epsilon = \left[1 + 2(1+\frac{\nu^2}{Q^2})\tan^2\frac{\theta}{2}\right]^{-1} \quad . \tag{13}$$

The cross section $d\sigma_V/d\Omega_\pi$ in Equation 11 depends only on the energy transfer $\nu = E - E'$ and Q^2. We have made preliminary measurements of the single π^+ production from the S_{11} resonance using the $p(e,e'\pi^+)n$ reaction during the E1-6 run period in CLAS [27]. The beam energy was $E = 5.75\ GeV$, $W = 1.535 \pm 0.1\ GeV$ and $Q^2 = 3.0 \pm 0.5\ (GeV/c)^2$. We use these results to estimate the production of π^+'s at the upgraded CLAS12 beam energy

$E = 11\ GeV$ and the same W and Q^2 region by correcting for differences in solid angle, photon flux factor Γ_V, CLAS and CLAS12 acceptances and luminosities, and running time. Once we have the π^+ production from the S_{11} for $Q^2 = 3.0 \pm 0.5\ (GeV/c)^2$ and $E = 11\ GeV$, we can then use a model to extrapolate to different Q^2 ranges. We assume the cross section has a dipole form so $\sigma \propto (1/(1 + Q^2/\Delta_S)^2)^2$ where $\Delta_S = 1.6\ (\mathrm{GeV/c})^2$. This assumption is based on an overview of the inclusive inelastic electron scattering [26]. The preliminary E1-6 results agree with the Reference [26] results at $Q^2 = 3.0\ (\mathrm{GeV/c})^2$ and the higher resonances measured in Reference [26] scale like the dipole form factor. These experimental results justifies the use of the event generator developed by the Genova group [32] since it assumes dipole behavior for the Q^2 dependence.

To summarize our method, we use the preliminary measurement of the single, positive pion production in CLAS at E = 5.75 GeV and $Q^2 = 3.0\ (\mathrm{GeV/c})^2$ to establish a normalization for CLAS12 measurement at E = 11.0 GeV and $Q^2 = 3.0\ (\mathrm{GeV/c})^2$ (with appropriate corrections for solid angle, acceptances, virtual photon flux, *etc.*). We then use the Genova event generator to predict the behavior at other Q^2. The π^+ production is simulated with the Genova event generator and the events filtered through the CLAS12 parameterized simulation FASTMC. We note here this is a conservative estimate since we consider only a single resonance (the S_{11}) in the simulation whereas we can use tagged neutrons from other resonances for our measurement of the neutron detection efficiency. We assumed 54 days of beam time for our calculations. See Section 3.5.3 for more details on the run-time statistics.

The results of our simulation of the neutron calibration reaction are shown in Figure 23 The left-hand panels shows the calculation for the range $Q^2 = 2 - 14\ (\mathrm{GeV/c})^2$. Neutrons

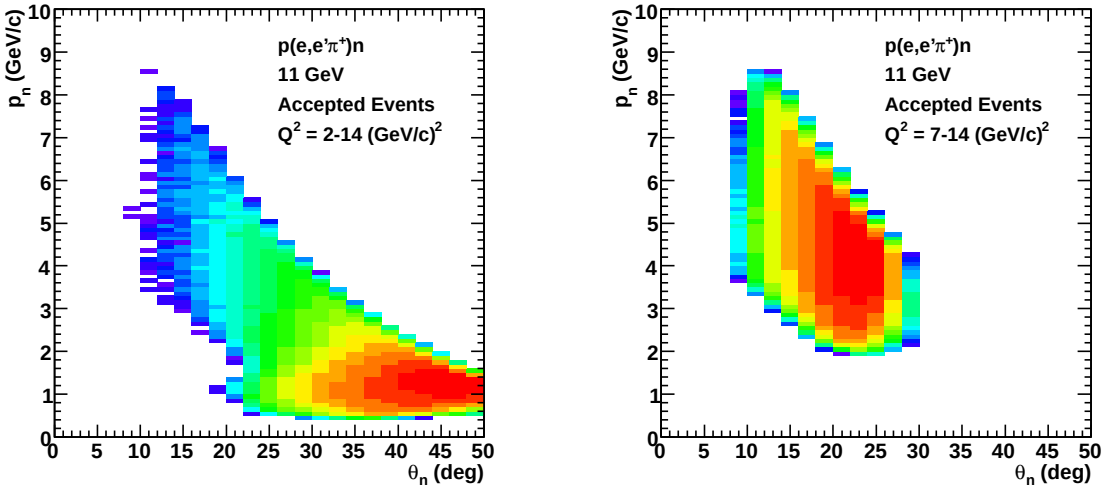

Figure 23: FastMC simulation of the $p(e, e'\pi^+)n$ reaction in CLAS12 for $E = 11$ GeV and a torus current of 2250 A for two different Q^2 ranges.

cover a wide angle range past $\theta_n = 40°$ (the limit of the forward detector in CLAS12) meaning we will be able to calibrate the large-angle portions of the calorimeter. To focus on the most

forward angles and highest energies we ran another simulation with $Q^2 > 7$ (GeV/c)^2. The results are shown in the right-hand panel. Notice that we cover close to the full range of momentum and angle that the production neutrons will reach as shown in Figure 22.

3.3.3 Proton Detection Efficiency

The proton efficiency measurement will be done using the hydrogen target and elastic *ep* scattering as a source of tagged protons. The kinematics of the scattered electron will be used to calculate the mass of the recoiling system W and a cut applied to select a proton. For these *ep* events, a track will be calculated going from the electron vertex, through the CLAS12 magnetic field, to a TOF paddle. If the track misses the fiducial region of CLAS12, it will be dropped. If the event is inside the fiducial region of CLAS12, it will be classified as a reconstructed event. If the same event is found to have a hit in the predicted TOF paddle, then it will be classified as a found event. The proton detection efficiency is the ratio of found to reconstructed events. These events will be subject to other cuts to reduce background and improve particle identification. The kinematics of elastic scattering from hydrogen is similar to the kinematics of quasielastic scattering from the proton in deuterium so we expect we will obtain adequate angle and momentum coverage for calibration.

3.4 Other Corrections

For the ratio method to be successful, careful matching of the geometric acceptance for $e-p$ and $e-n$ events from deuterium must be done. To make sure the proton and neutron acceptances are equal, a common fiducial region will be required for both nucleons. This can be done event-by-event in the following manner. The expected 3-momentum of the neutron or proton is determined from the electron kinematics assuming elastic scattering from a stationary nucleon. The effect of the internal motion of the nucleons in deuterium is discussed below. Assuming the event has a neutron, a ray is drawn from the electron vertex out to the TOF or EC systems and required to be in the respective fiducial region of the TOF or EC. Next, the event is assumed to have a proton and the track 'swum' from the electron vertex, through the magnetic field of CLAS12, to the TOF system; again requiring that it fall in the fiducial region of CLAS12. If either one of these conditions (neutron or proton predicted to be in the CLAS12 fiducial region based on the electron kinematics) is not met, then the event will be dropped. If both conditions are met, then the event is searched for a neutron or proton in the predicted location. This analysis will ensure the neutron and proton have the same geometric acceptance.

There are other corrections to R which must be considered in this experiment. The Fermi motion of the nucleons bound inside the deuteron can push events to different scattering angles so that they do not fall in the predicted detector component and could be lost. For the CLAS G_M^n experiment we have simulated this effect and found the contribution to the systematic uncertainty in the neutron magnetic form factor was less than 1%. The uncertainty on this correction was found to be small by using drastically different physics models in the event generator for the simulation and getting similar results in the correction to the ratio R. Radiative corrections will also be applied in this experiment. For the CLAS G_M^n analysis we have calculated radiative corrections using a modified version of the code

Quantity	2.6 GeV	4.2 GeV	Quantity	2.6 GeV	4.2 GeV
Calorimeter neutron efficiency parameterization	< 1.5	< 1.0	TOF neutron efficiency parameterization	< 2.0	< 2.0
proton σ	< 1.0	< 1.5	G_E^n	< 0.5	< 0.7
neutron accidentals	< 0.07	< 0.3	neutron MM cut	< 0.5	< 0.07
neutron proximity cut	< 0.22	< 0.15	proton efficiency	< 0.3	< 0.35
Fermi loss correction	< 0.8	< 0.9	θ_{pq} cut	< 0.4	< 1.0
Nuclear Corrections	< 0.17	< 0.2	Radiative corrections	< 0.05	< 0.06

Table 2: Upper limits on the estimated systematic errors in % for different contributions.

EXCLURAD written by Afanasev, *et al.* for exclusive electro-nuclear reactions [19, 20]. The corrections can be large (up to 30%) for $Q^2 < 4$ GeV^2 for the individual cross sections σ_{ep} and σ_{en}, but these radiative corrections to R nearly cancel in the $e-n/e-p$ ratio (to less than 0.2%) [3, 20]. The quantity of interest in this project is the ratio of free $e-n$ scattering to $e-p$ scattering so corrections for the effect of nuclear binding in the deuteron must be applied. For the CLAS G_M^n analysis we used two calculations from S. Jeschonnek and H. Arenhoevel to estimate these effects and both were found to be small (less than 0.3%) [3]. For this experiment, a similar calculation by Jeschonnek showed a correction factor of less than 0.1% [21].

3.5 Experimental Uncertainties

An essential goal of this experiment is to achieve low ($\approx 3\%$) uncertainties on G_M^n. This is about the same level of precision we reached in the CLAS G_M^n measurement with the electromagnetic calorimeter for neutron detection. The uncertainties on the TOF measurements of the neutrons were higher. A summary of the uncertainties for the CLAS measurement of G_M^n is shown in Table 2. The largest contributor to the systematic uncertainty at both CLAS energies was the determination of the neutron detection efficiency. Those measurements are in a neutron momentum range where the detection efficiency is changing rapidly (see Figure 24) so fits to the data to extract the efficiency curve had significant ($\approx 1-2\%$) errors. We expect to reach similar levels of precision with CLAS12. Much of the new data will be at higher neutron momentum where the efficiency curve will be flatter and less sensitive to variations in neutron momentum. The uncertainties in the other elastic form factors used to extract G_M^n in the ratio are the next largest contributor to the systematic uncertainty ($\approx 1-1.5$ %).

The rest of the sources of uncertainty in the CLAS measurement in Table 2 are small. None of these sources showed signs of significant increases with higher beam energy so we

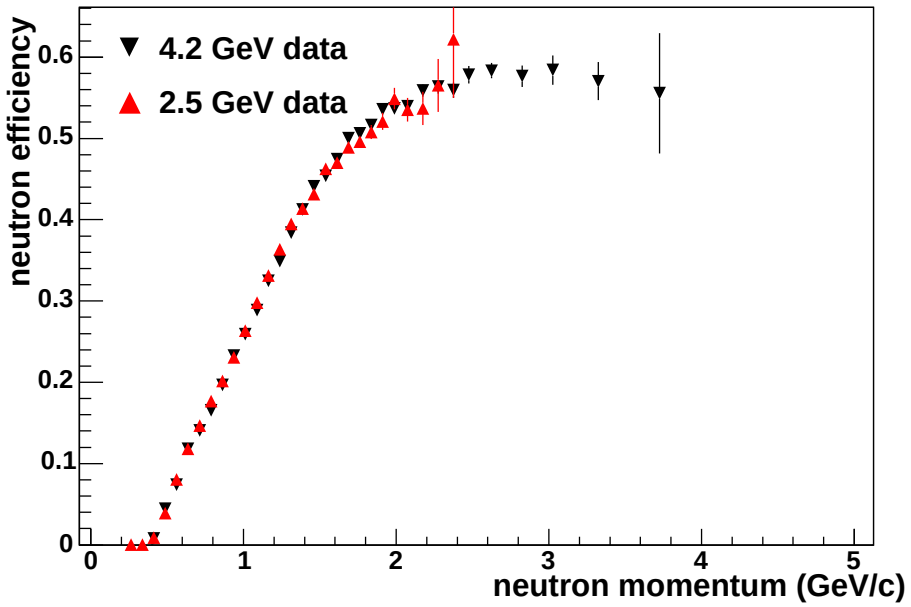

Figure 24: A comparison of the neutron detection efficiency measured in the EC from the CLAS G_M^n, as measured at two different beam energies. In this figure, the efficiency has been integrated over all six sectors [3].

are encouraged that we can achieve the desired precision. In this section we will discuss the method for determining the uncertainty in G_M^n and focus on estimates of the effect of the parameterization of the neutron detection efficiency and the other elastic form factors which were the largest contributors to the total systematic uncertainty.

In Equation 9 we defined the ratio R in terms of the elastic form factors. Solving that equation for G_M^n gives

$$G_M^n = \pm\sqrt{\left[R\left(\frac{\sigma_{mott}^p}{\sigma_{mott}^n}\right)\left(\frac{1+\tau_n}{1+\tau_p}\right)\left(G_E^{p\,2} + \frac{\tau_p}{\varepsilon_p}G_M^{p\,2}\right) - G_E^{n\,2}\right]\frac{\varepsilon_n}{\tau_n}} \tag{14}$$

where the subscripts refer to the separate quantities for protons and neutrons. For the purpose of evaluating systematic errors, the above equation can be simplified by making the approximations

$$\frac{\sigma_{mott}^p}{\sigma_{mott}^n} \approx 1 \tag{15}$$

$$\frac{1+\tau_n}{1+\tau_p} \approx 1 \tag{16}$$

The neutron magnetic form factor expression becomes

$$G_M^n = \sqrt{\left[R\,\sigma_R - G_E^{n\,2}\right]\frac{\varepsilon}{\tau}} \tag{17}$$

where $\sigma_R = {G_E^p}^2 + \frac{\tau_p}{\varepsilon_p}{G_M^p}^2$ is the reduced proton cross section. The standard propagation of errors formula is applied.

$$(\delta G_M^n)^2 = \left(\frac{\partial G_M^n}{\partial \sigma_R}\right)^2 (\delta\sigma_R)^2 + \left(\frac{\partial G_M^n}{\partial G_E^n}\right)^2 (\delta G_E^n)^2 + \sum_i \left(\frac{\partial G_M^n}{\partial f_i}\right)^2 (\delta f_i)^2 \tag{18}$$

The f_i are the set of all other parameters the ratio R depends on (efficiencies, radiative corrections, and so on). We will use this result in our analysis below.

3.5.1 Neutron Detection Efficiency Parameterization

The uncertainty in the parameterization of the neutron detection efficiency is the largest single source of uncertainty in the G_M^n measurement. To estimate that uncertainty in the proposal we have done the following.

1. We start with function that will qualitatively describe the neutron detection efficiency (NDE). See Figure 24 which shows the measured NDE from the CLAS G_M^n measurement. However, we avoid a simple polynomial because that is the function that was used to fit the NDE in our analysis and could bias the result. We chose to use the function

$$\epsilon_n = S \times \left(1 - \frac{1}{1 + \exp(\frac{p_n - p_0}{a_0})}\right) \tag{19}$$

   where S is the height of the plateau in NDE for $p_n > 2\ GeV/c$, p_0 is a constant representing the position of the middle of the rapidly rising portion of the NDE, and a_0 controls the slope in the increasing NDE region. The points in Figure 25 fall along this curve.

2. We use the momentum distribution of simulated neutrons assuming NDE=1 and apply the source NDE function from above (Equation 19) to obtain the number of accepted neutrons as a function of momentum. The square root of this number gives us the uncertainty in that neutron momentum bin.

3. Monte Carlo events are generated in each momentum bin with a Gaussian distribution with the centroid and width from the previous step.

4. We fit the distribution with the original source NDE in Equation 19 (which simply recovers the original parameters) and with a third-order polynomial in p_n with a plateau (we will refer to this function as the CLAS-G_M^n fit). The results are shown in Figure 25. Notice the small differences between the red curve (original source NDE) and the green one (CLAS-G_M^n curve). We chose the original source function so that it would have the same features as the measured neutron detection efficiency, but would not necessarily make a perfect fit to the simulated neutron detection efficiency.

5. We then do two calculations. In both we use the source NDE function above (the red curve in Figure 25) to generate the events. In one calculation we use the functional form of the original source NDE to correct the neutron yield for the NDE in the analysis.

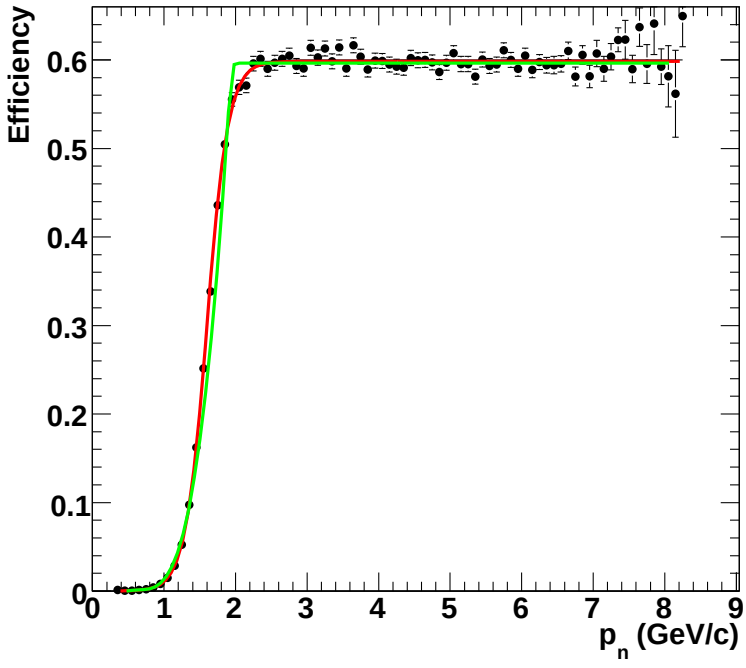

Figure 25: Monte Carlo simulation of the neutron detection efficiency along with two fits to the simulated data. The red curve is a fit to the simulated neutron detection curve using Equation 19; the green curve is a third-order polynomial at low p_n and has a constant value at high p_n. The boundary between the two parts of the green curve is varied to find the best fit.

In the second calculation we use the CLAS-G_M^n fit in the analysis code to correct the neutron yield for the neutron detection frequency. We use the original source NDE function to throw the events in each case.

6. Last, we calculate $R = e - n/e - p$ for each case and take the difference between the two. We call this δR_{NDE}. To calculate the uncertainty in G_M^n caused by δR_{NDE} we go back to the third term on the right-hand-side of Equation 18. For the contribution of the parameter f_i to the overall uncertainty is

$$(\delta G_M^n)_i^2 = \left(\frac{\partial G_M^n}{\partial f_i}\right)^2 (\delta f_i)^2 \tag{20}$$

which can be rewritten as the following.

$$(\delta G_M^n)_i^2 = \left(\frac{\partial G_M^n}{\partial R_{NDE}}\frac{\partial R_{NDE}}{\partial f_i}\right)^2 (\delta f_i)^2 \tag{21}$$

$$= \left(\frac{\sigma_p \epsilon}{2 G_M^n \tau}\frac{\partial R_{NDE}}{\partial f_i}\right)^2 (\delta f_i)^2 \tag{22}$$

We can approximate the partial derivative as

$$\frac{\partial R_{NDE}}{\partial f_i} \approx \frac{\delta R_{NDE}}{\delta f_i} \tag{23}$$

and use $G_M^n \approx \mu_n G_D$ to obtain the following result that can be used to calculate the effect of δR_{NDE} on the uncertainty in G_M^n.

$$\left(\frac{\delta G_M^n}{G_M^n}\right)^2 = \left(\frac{\sigma_p \epsilon}{2\mu_n^2 G_D^2 \tau}\right)^2 (\delta R_{NDE})^2 \tag{24}$$

The result is shown in Figure 26 for the relative uncertainty on G_M^n. The error bars are statistical ones from the Monte Carlo calculation. The difference in the two parameterizations of the NDE is roughly constant with Q^2 and less than 1.0% across the full range. The size of this effect is comparable to what was observed in the CLAS G_M^n measurement.

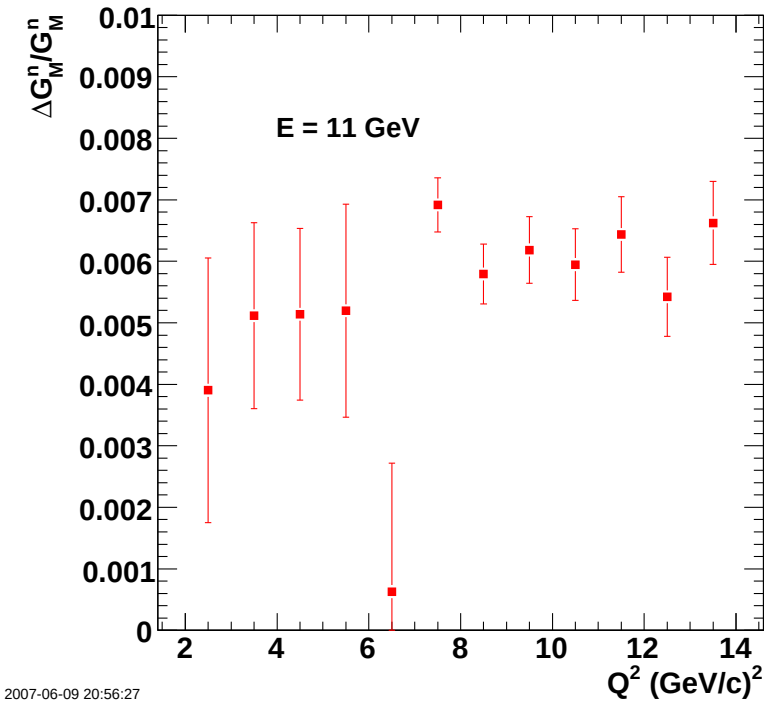

Figure 26: Relative difference in G_M^n between the two forms of the neutron detection efficiency in the analysis.

3.5.2 Knowledge of Other Elastic Form Factors

The fractional error on G_M^ndue to uncertainty in the proton reduced cross section is the following.

$$\frac{(\partial G_M^n)_R}{G_M^n} = \frac{1}{2{G_M^n}^2} R \frac{\varepsilon}{\tau} \delta\sigma_R \tag{25}$$

To estimate this contribution, we assume $G_M^n \approx \mu_n G_D$. The ratio R is taken as the free neutron to proton [37] cross section ratio and $\delta\sigma_R$ as the difference between the Arrington-Melnitchouk [38] (AM) and Bosted [36] parameterizations:

$$\delta\sigma_R = \sigma_R^{Arrington-Melnitchouk} - \sigma_R^{Bosted} \tag{26}$$

Several parameterizations are available on the market but only few are results of cross section fits. The parameterizations that are based on form factor measurement fits should not be used to evaluate the systematic error in G_M^n due to uncertainty in proton cross section. The reason is that they do not take into account the two photon exchange contribution. In that case we are left only with three parameterizations [36],[37],[38] to choose from. The AM [38] parametrization is an update for the Arrington one [37]. Therefore we have decided to compare the AM parametrization to the Bosted one [38]. We used the Kelly parametrization [39] to evaluate R since none of the above parameterizations provide information on the neutron cross section. The difference $\delta\sigma_R$ is shown in the upper plot of Figure 27. Using that $\delta\sigma_R$, the estimated systematic uncertainty on G_M^n caused by the uncertainty in σ_R can be determined. Both the relative size of the difference in the two parameterizations and the fractional uncertainty on G_M^n expressed as a percentage are shown in the lower plot of Figure 27. The obtained systematics are realistic for Q^2 below 6 GeV, where measurements of the proton elastic cross sections are available with good precision. For higher Q^2 values, few measurements exist and those have large errors. Therefore all fits give good χ^2 and the difference between parameterizations are meaningless. Nonetheless, measurements of the proton elastic cross section are expected to be the first available data from the JLab 12 GeV upgrade since this reaction is also used for calibration purposes. A 4% *ep* elastic cross section measurements will lead to roughly 2% on the G_M^nsystematic error due to uncertainty on the proton cross section. We expect to reduce this error below 1.5% by combining different measurements.

The fractional error on G_M^n due to the uncertainty in the neutron electric form factor is

$$\frac{(\partial G_M^n)_E}{G_M^n} = \frac{G_E^n}{{G_M^n}^2}\frac{\varepsilon}{\tau}\delta G_E^n \tag{27}$$

To estimate this contribution, we assume: $G_M^n \approx \mu_n G_D$, and use the Kelly parametrization for G_E^n. We take $\delta G_E^n$to be the difference between Kelly and BBBA05 parameterizations [40]

$$\delta G_E^n = G_E^{n\,Kelly} - G_E^{n\,BBBA05} \tag{28}$$

The Kelly and BBBA05 results are shown in Figure 28. Due to the lack of measurements for G_E^n above Q^2 of 1.5 GeV^2, the two parameterizations have very different behaviors. The BBBA05 use high Q^2constraints based on QCD sum rule which cause G_E^n to die off much more quickly at high Q^2 than does the Kelly parametrization. Fortunately, the contribution of G_E^n is expected to decrease with increasing Q^2 because it is already measured to be small and it is kinematically suppressed. We took these two extreme behaviors of existing G_E^n parametrization in order to draw the worst case scenario. The difference δG_E^n is plotted in the upper plot of Figure 29. The fractional uncertainty on G_M^n expressed as a percentage are shown in the lower plot of Figure 29. These errors are larger at low Q^2region where the

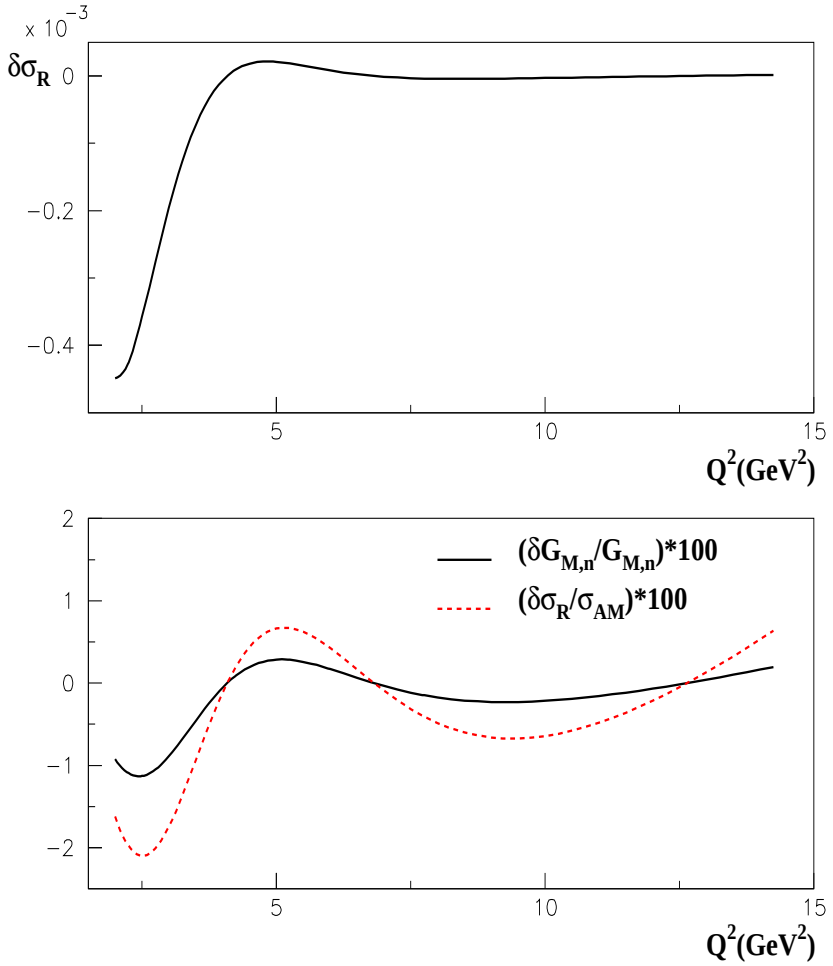

Figure 27: The upper plot is the difference in the proton reduced cross section as determined from AM and Bosted parameterizations as a function of Q^2. The lower plot is the systematic error on G_M^ndue to the uncertainties in the reduced proton cross section (solid curve) and the relative difference in the proton reduced cross section, as determined for AM and Bosted parameterizations scaled to the AM result (dashed curve)

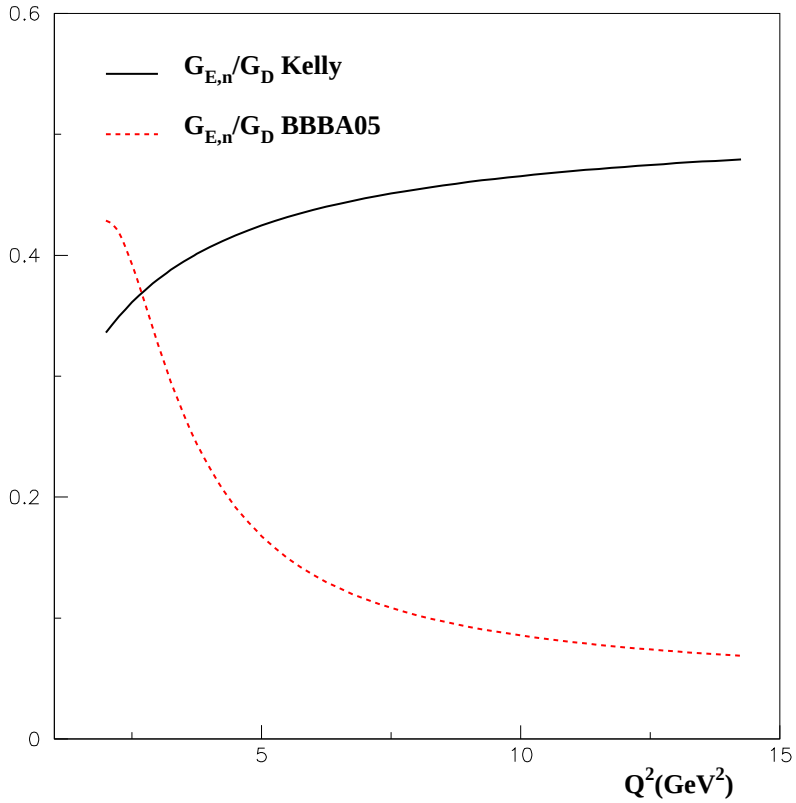

Figure 28: The neutron electric form factor from Kelly and BBBA05 parameterizations as a function of Q^2

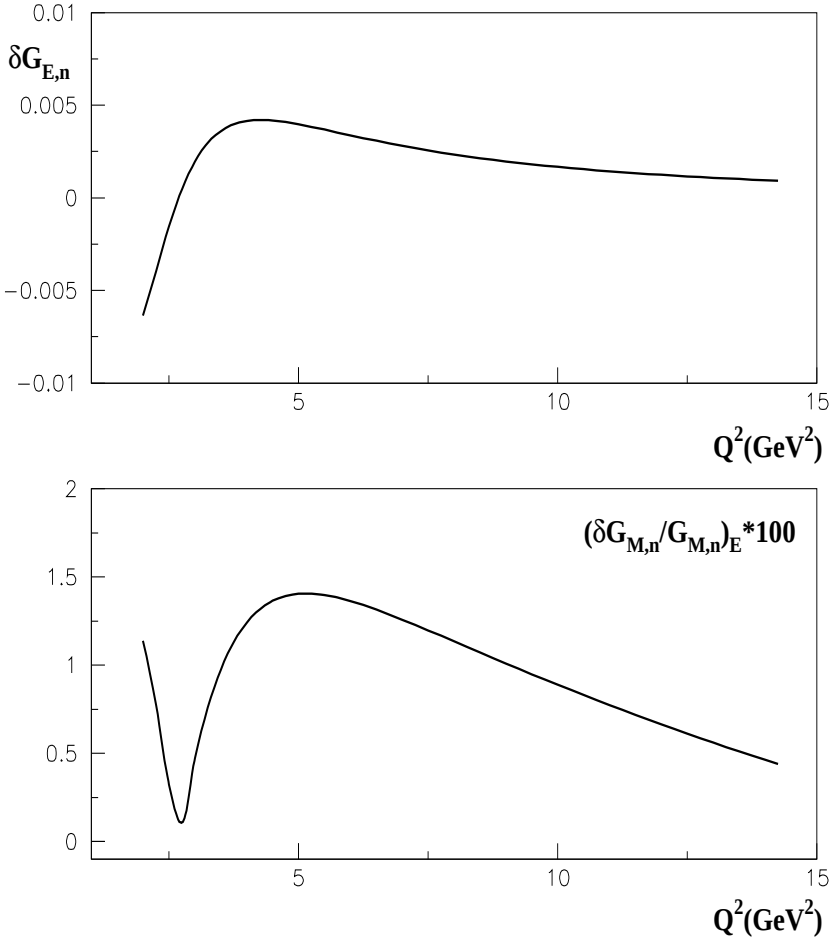

Figure 29: The upper plot plot is the difference in the neutron electric form factor as determined from Kelly and BBBA05 parameterizations as a function of Q^2. The lower plot is the systematic error on G_M^ndue to the uncertainties in G_E^n as a function of Q^2

G_E^n values are larger. Taking into account the measurements of Hall A experiment E02-013 that are being analyzed, the errors in the Q^2 region between 1.7 $(GeV/c)^2$ and 3.4 $(GeV/c)^2$ are expected to drop by a factor of 3. Similar measurements for Q^2 of 4.5 $(GeV/c)^2$ are being planned. In addition, measurements at $Q^2 = 7.5$ $(GeV/c)^2$are part of the JLab 12 GeV program. If performed, the largest error in the neutron magnetic form factor due to the uncertainty in G_E^n will not exceed 0.5%.

3.5.3 Statistical Uncertainties

We have estimated the rate of the $D(e,e'p)n$ and $D(e,e'n)p$ reactions to determine how much beam time would be needed to obtain data of similar quality to the CLAS G_M^n measurement. The primary consideration is to obtain an adequate number of events so the statistical uncertainty does not dominate the systematics ones. We used Equations 3-6 and made the following assumptions about the form factors

$$G_E^p \approx G_D = \frac{1}{(1+Q^2/\Delta)^2} \qquad G_M^p \approx \mu_p G_D \qquad G_M^n \approx \mu_n G_D \qquad G_E^n = \frac{\mu_n \tau G_D}{1+\eta\tau} \tag{29}$$

where μ_n and μ_p are the neutron and proton magnetic moments, $\Delta = 0.71$ $(GeV/c)^2$, and $\eta = 5.6$ (from the Galster parameterization [9]). The acceptances are shown in Figures 12 (protons) and 17 (neutrons). The anticipated luminosity is $0.5 \times 10^{35}\ cm^{-2}s^{-1}$ for the dual-cell target. The length of each target cell is 2.0 cm. We have to compensate for two effects which reduce the usable data sample from the production and calibration targets. As we did in the CLAS measurement, we will apply cuts on the vertex position of the tracks to remove contributions from the aluminum windows of the target cells. These cuts effectively make the target shorter. Based on expectations for the CLAS12 vertex resolution we anticipate using a cut of about 1.5 mm on the two windows on each cell which requires a factor of about 15% to compensate for the loss (3 mm out the total of 20 mm in the target). The second effect is from events produced in the windows that add to the total luminosity and effectively reduce the beam current on the production and calibration targets. The amount of material in the aluminum windows is about 3% of the material in the deuterium target. Without these two effects, we would obtain the desired statistics shown in Table 3 in 45 days. To compensate for the two effects requires a total of 54 days. We are also requesting one day for diagnostic tests like empty target runs and straight-track runs and one more day for interchanging the hydrogen and deuterium targets. In the last procedure, we would switch the liquids in each cell to test for any measurable effects due to the different target positions. The total request is for 56 days.

The beam time request for this experiment is 56 days of 11.0 GeV beam at a luminosity per nucleon of of $0.5 \times 10^{35}\ cm^{-2}s^{-1}$. The expected count rates, cumulative number of events and statistical uncertainty for a bin size of ± 0.5 $(GeV/c)^2$ around each value of Q^2 for quasielastic scattering are given in Table 3. From the table, the precision of the experiment will be limited by systematic uncertainties at low Q^2. At high Q^2 the experiment is near the limit where statistical uncertainty begins to dominate.

The results are shown in another form in Figure 30 along with existing data on G_M^n [23]. The blue, open points show the expected Q^2 coverage and uncertainties for 56 days of beam time. The uncertainties include both statistical and systematic uncertainties. The

Q^2 $(GeV/c)^2$	Proton Rate (s^{-1})	Neutron Rate (s^{-1})	Proton Counts	Proton Error (%)	Neutron Counts	Neutron Error (%)
2.5	0.39	2.	7.56×10^5	0.115	3.94×10^6	0.0504
3.5	4.10	2.8	7.88×10^6	0.036	5.44×10^6	0.0429
4.5	7.50	2.2	1.45×10^7	0.026	4.2×10^6	0.0488
5.5	2.80	0.91	5.41×10^6	0.043	1.77×10^6	0.0752
6.5	1.10	0.32	2.06×10^6	0.070	6.19×10^5	0.127
7.5	0.430	0.12	8.33×10^5	0.110	2.4×10^5	0.204
8.5	0.190	0.052	3.64×10^5	0.166	1.01×10^5	0.315
9.5	0.090	0.023	1.75×10^5	0.239	4.46×10^4	0.473
10.5	0.0460	0.011	8.93×10^4	0.335	2.06×10^4	0.696
11.5	0.0220	0.0051	4.24×10^4	0.486	9.82×10^3	1.01
12.5	0.0110	0.0024	2.05×10^4	0.699	4.76×10^3	1.45
13.5	0.0051	0.0012	9.95×10^3	1.0	2.32×10^3	2.08

Table 3: Rates and statistical uncertainties for quasielastic scattering.

red points at low Q^2 are the preliminary results of the measurement of G_M^n by Lachniet, *et al.* [3]. It is worth noting the large overlap of the CLAS12 measurement with the CLAS one. This overlap gives us another useful consistency check. The proposed measurement will significantly expand our understanding of the neutron magnetic form factor.

3.6 Relationship to Existing Experiments

All nucleon form factor measurements are closely connected and this proposed one is part of a broad assault on the nucleon elastic form factors in the current 6-GeV program and the 12-GeV Upgrade at JLab. We propose to extend the existing data set for G_M^n from the current limit of $Q^2 \approx 4.5$ (GeV/c)^2 up to $Q^2 \approx 14$ (GeV/c)^2. The proposed measurement will also overlap the CLAS measurement and provide an important consistency check. The extraction of the neutron magnetic form factor depends to some extent on the proton elastic cross section and the neutron electric form factor. A proposal [41] to measure the proton elastic cross section with a precision better than 2% in Hall A after the JLab 12 GeV Upgrade has been planned for submission to PAC32. These measurements are also expected to extract the proton magnetic form factor for Q^2 up 17 GeV^2. At 6 GeV, E04-108 [42] is an approved experiment that is scheduled to run this year in Hall C. The goal here is to measure the ratio G_E^p/G_M^p for Q^2 of 5.2, 7.1 and 8.6 GeV^2. An extension to Q^2 of 15 GeV^2 for the 12 GeV Upgrade was suggested in LOI-07-013 using SHMS and BigCAL in Hall C [43]. New results for G_E^n are expected soon from Hall A experiment E02-013 [44]. The measured Q^2 values are 1.2, 2.48 and 3.43 GeV^2. There is also an effort investigating the possibility of measuring G_M^n at 6 GeV in Hall A [45].

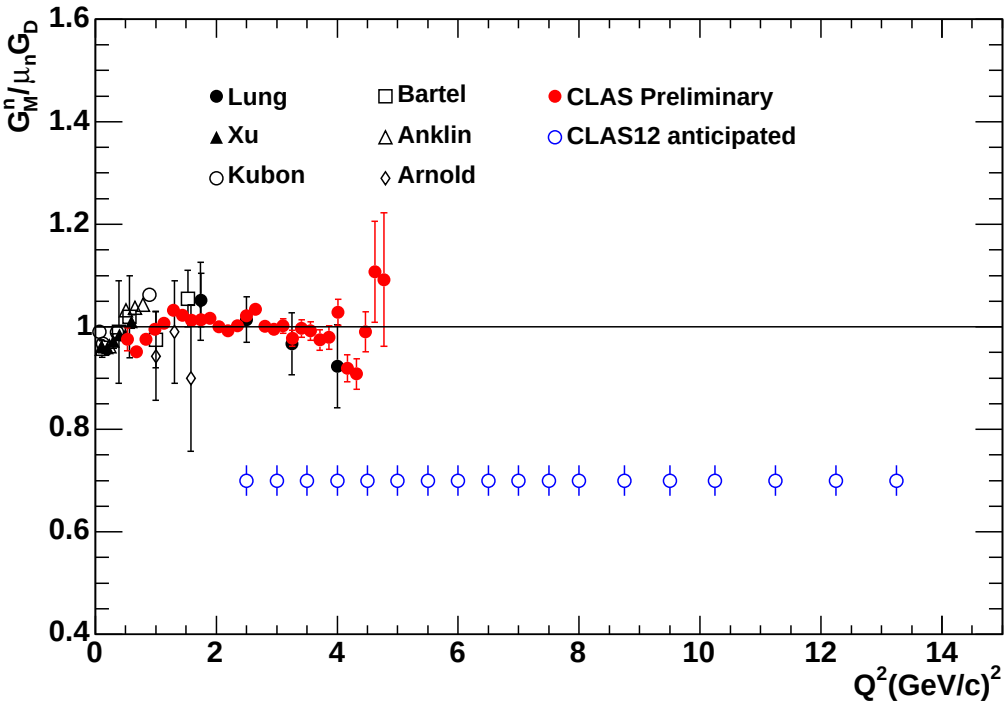

Figure 30: Selected data and estimated results for the neutron magnetic form factor G_M^n for 45 days of running time with CLAS12 (blue, open circles) in units of $\mu_n G_D$ as a function of Q^2. The red circles at low Q^2 represent the preliminary results from the E5 experiment [3, 23].

3.7 Summary and Request

We propose to measure the magnetic form factor of the neutron using the 11 GeV electron beam in the upgraded CEBAF and CLAS12 detector. The measurement will be in the range $Q^2 = 2 - 14$ GeV^2 with a systematic uncertainty of 3%. The neutron's magnetic form factor is one of the fundamental quantities of nuclear physics and its value is an important constraint for the newly-developed generalized parton distributions that hold the promise of dramatically expanding our understanding of the nucleon. The form factors are also important challenges for lattice QCD to meet. This measurement is part of a broad assault on the four elastic nucleon form factors at Jefferson Lab.

We will use the ratio of elastic $e-n$ to elastic $e-p$ scattering on deuterium described in Section 3. The ratio method is less vulnerable to uncertainties than previous methods and we will have consistency checks between different detector components (*e.g.*, the TOF and EC) and a large overlap with our previous CLAS measurements. Precise measurements of G_M^n have already been made by our group and others at lower Q^2 [3, 5, 6, 7]. The group of international CLAS collaborators from universities and national laboratories that are part of this proposal have made significant commitments to the 12-GeV Upgrade program.

We request 56 days of beam time at an energy of 11.0 GeV and a luminosity per nucleon

of $0.5 \times 10^{35}\ cm^{-2}s^{-1}$. We anticipate we will obtain adequate statistics across the full Q^2 range so the systematic uncertainties will not be dominated by statistical ones.

4 Technical participation of research groups

4.1 University of Richmond

The University of Richmond group is actively involved in this proposal, as well as in one other proposal using CLAS12 that was approved by PAC30 (PR12-06-117).

Among CLAS12 baseline equipment, the group intends to take responsibility for the design, prototyping, development and testing of software for event simulation and reconstruction. One faculty member along with 2-3 undergraduates each year are likely to work at least part time on this project in the next few years. Work has begun during the summer of 2007 to develop software to enable users to pass simulated events to SIM12, the GEANT4-based, CLAS12, simulation package. The group has a 50-CPU computing cluster solely for nuclear physics supported by a linux-trained, technical staff member. The cluster was funded by NSF and the University. The University also supports routine travel to Jefferson Lab and undergraduate summer stipends. Funding for the group is from DOE. Additional sources of funding will be sought as appropriate.

4.2 Old Dominion University

The Old Dominion University group (Prof. Amarian, Bültmann, Dodge, Kuhn and Weinstein) is actively involved in several other proposals using CLAS12, in addition to the present one. Other members of our group are pursuing 12-GeV proposals for Hall A, but their contributions are not included here. In support of our strong interest in Physics with CLAS12, our group has taken on responsibility for a major component of the CLAS12 baseline equipment. The group has begun work on the design and prototyping of the new Region I drift chambers for CLAS12. This work has involved the faculty, two graduate students, several undergraduate students and a technician. We have set up a data acquisition system to test various prototype chambers and have been involved and the detailed engineering design of the chamber, parts of which have already entered the procurement phase.

As a result of an in-depth review of the whole CLAS12 tracking project (of which one of us is the co-organizer), it was decided that our group will ultimately design, prototype, construct and test the Region 2 Drift Chambers. A Memorandum of Understanding between ODU and JLab to this end has been executed. We expect to continue our strong commitment of manpower to this project. Funding for the group is from DOE and from the university (75% of research faculty salary + one regular faculty summer salary + 50% of the technician). The university has also provided 6000 square feet of high bay laboratory space with clean room capabilities for our use. We will seek other sources of funding as appropriate. Gail Dodge is the chair of the CLAS12 Steering Committee and the user coordinator for the CLAS12 tracking technical working group. Sebastian Kuhn is the user coordinator for beamline elements. Beyond the baseline equipment, the group is also interested in working on improvements to the existing BoNuS detector and on polarized targets.

4.3 Argonne National Laboratory

Argonne National Laboratory Medium Energy group is actively involved in this proposal, as well as other proposals using CLAS12. Among CLAS12 baseline equipment, the group intends to take responsibility for the design, prototyping, construction and testing of the high threshold Cerenkov counter. Three research staff and two engineers are likely to work at least part time on this project in the next few years. Funding for the group is from DOE. Additional sources of funding will be sought as appropriate. Beyond the baseline equipment, the group is also interested in exploring the possibility of building a RICH detector for CLAS12.

4.4 Union College

The Union College group is actively involved in this proposal and other parts of the CLAS12 physics program. The group plans to work with the CLAS12 software group on the development of software for analysis, simulation, and controls. One faculty member and 2-3 students will work at least part time on this project over the next few years. The group has a 20-CPU Beowulf cluster provided by Union College to support the work at Jefferson Lab. The College also provides stipends for undergraduate students involved in research during the summer. The group is also funded by DOE.

4.5 University of New Hampshire

The University of New Hampshire is a supporter of this proposal as well as actively involved in other proposals using CLAS12.

The UNH group is committed to significant contributions in the development of the CLAS12 software. Maurik Holtrop is currently chair of the CLAS12 GEANT4 simulation group to which one of the UNH post-doctoral fellows (Hovanes Egiyan) is also contributing. Since currently the main software efforts for CLAS12 are in the area of simulation we are also part of and contributing to the general CLAS12 Software group. Current manpower commitments to this effort are 0.15 FTE of a faculty member and 0.4 FTE of one post-doc. We expect to increase this effort as our CLAS activities wind down and our CLAS12 activities pick up and we expect to attract some talented undergraduate students to this project.

Among CLAS12 baseline equipment, the group intends to take responsibility for design, prototyping, construction, and testing of the silicon vertex detector and perhaps the inner detector's silicon tracking detectors. Faculty member Maurik Holtrop is likely to work at least part time on this project in the next few years and is likely to be joined by Jim Connel, a cosmic ray experimentalist with a background in nuclear physics, who is very interested in joining the vertex detector project. He has considerable experience with silicon detectors for space observations. Funding for the group is from DOE and additional sources of funding will be sought for this project to bring aboard Dr. Connel. If funded we are likely to attract a post-doc, graduate students, and one or two undergraduate students to this project.

Beyond the baseline equipment, the group is also interested in exploring an extended inner calorimeter for CLAS12.

4.6 DAPNIA/SPhN-Saclay

The DAPNIA/SPhN-Saclay group expressed interest in this proposal. It is actively involved in two proposals using CLAS12, and one other proposal for Hall A.

Among CLAS12 baseline equipment, the group intends to take responsibility for the design, prototyping, construction and testing of the central tracker (both the cylindrical part and the forward part). The group has started working on an option based on cylindrical Micromegas detectors. Provided this is shown to work as designed, the group anticipates that this option will be examined in comparison with the Silicon Strip tracker, toward the end of 2007 or the beginning of 2008. Four research staff members and four technicians/engineers are likely to work at least part time on this project in the next few years. Funding for the group is from CEA-France. Additional sources of funding (ANR-France, European Union 7th PCRD) will be sought as appropriate.

In case the Micromegas option is not suitable, or not selected for valid reasons, the group would study other technical participation in the CLAS12 baseline equipment.

Beyond the baseline equipment, the group is also interested in exploring neutral particle detection (mostly neutrons) in the central detector of CLAS12, in the so far empty space between the TOF scintillators and the solenoid cryostat.

5 References

[1] M.N. Rosenbluth, Phys. Rev. **79** (1950) 615.

[2] C.E. Hyde-Wright and K.deJager, Ann. Rev. Nucl. Part. Sci. **54** (2004) 54.

[3] J.D. Lachniet, *A High Precision Measurement of the Neutron Magnetic Form Factor Using the CLAS Detector*, thesis, Carnegie Mellon University.

[4] W. Brooks and M.F. Vineyard, *The Neutron Magnetic Form Factor from Precision Measurements of the Ratio of Quasielastic Electron-Neutron to Electron-Proton Scattering in Deuterium*, Jefferson Lab Experiment E94-017 1994.

[5] H. Anklin, *et al.*, Phys. Lett. B, **336** (1998) 313.

[6] H. Anklin, *et al.*, Phys. Lett. B, **428** (1998) 248.

[7] G. Kubon, *et al.*, Phys. Lett. B, **524** (2002) 26.

[8] E.E.W. Bruins, *et al.*, Phys. Rev. Lett. **75** (1995) 21.

[9] S. Galster, H. Klein, J. Moritz, K.H. Schmidt, D. Wegener, and J. Blechwenn, Nucl. Phys. B32, (1971) 221.

[10] G.P. Lepage and S.J. Brodsky, Phys. Rev. D, **22** (1980) 2157.

[11] M.K. Jones, *et. al.*, Phys. Rev. Lett. **84** (2002) 1398.

[12] V. Punjabi, *et al.*, Phys. Rev. C **64** (2001) 038202.

[13] O. Gayou, *et al.*, Phys. Rev. Lett. **88** (2002) 092301.

[14] J.D. Ashley, D.B. Leinweber, A.W. Thomas, and R.D.Young, Eur. Phys. J A **19** s01 (2004) 9.

[15] *Science Review of the Proposed 12 GeV CEBAF Upgrade*, US Department of Energy, Office of Nuclear Physics (2005).

[16] M. Guidal, M.V.Polyyakov, A. V. Radyushkin, and M.Vanderhaeghen, Phys. Rev. **D58**, (2005) 054013.

[17] M. Diehl, Th. Feldmann, R. Jakob, and P. Kroll, Eur.Phys.J.C **39** (2005) 1.

[18] *Pre-Conceptual Design Report (pCDR) for The Science and Experimental Equipment for The 12 GeV Upgrade of CEBAF*, Jefferson Lab report 2004.

[19] A. Afanasev, I. Akushevich, V. Burkert, and K. Joo, Phys.Rev., **D66** (2002) 074004.

[20] G.P. Gilfoyle and A. Afanasev, 'Radiative Corrections for Deuteron Electro disintegration', CLAS-Note 2005-022.

[21] S. Jeschonnek, private communication.

[22] S. Rock, *et. al.*, Phys. Rev. Lett. **49** (1982) 1139.

[23] D. Abbott, *et al.*, *Hall B 12 GeV Upgrade Preconceptual Design Report*, Thomas Jefferson National Accelerator Facility (2002).

[24] F. Gross, *Relativistic Quantum Mechanics and Field Theory*, Wiley, 1993.

[25] E.J.Brash, A.Kozlov, S.Li, and G.M.Huber, Phys. Rev. **C66**, (2002) 051001.

[26] P. Stoler, Phys. Rep., **226**, 103 (1993).

[27] K. Park, private communication.

[28] L.M.Stuart, *et al.*, Phys. Rev. **D58** (1998) 032003.

[29] M.Mestayer, 'Drift Chambers for CLAS 12', CLAS12 Drfit Chamber Review, March 7, 2007.

[30] N.Dashyan, Private communication.

[31] W.K. Brooks, 'Specifications for the E5 ('dual-cell') Target', CLAS-Note 2001-015, June 1, 1999.

[32] M.Ripani and E.M.Golovach based on P.Corvisiero, *et al.*, Nucl. Instr. and Meth., **A346**, 433 (1994).

[33] Comp. Phys. Comm., 82 (1994) 74.

[34] S.Boffi, C.Giusti, F.D.Pacati, and M.Radici, 'Electromagnetic Response of Atomic Nuclei', Clarendon Press (1996).

[35] Harut Avakian, private communication.

[36] P. Bosted, Phys. Rev. C 51, 409 (1995).

[37] J. Arrington, Phys. Rev. C 69, 022201(R) (2004).

[38] J. Arrington, W. Melnitchouk, private communication.

[39] J. J. Kelly, Phys. Rev, C 70, 068202 (2004).

[40] R. Bardford, A. Bodek, H. Budd and J. Arrington, hep-ph/0602017.

[41] J. Arrington, Private communication.

[42] C.F. Perdrisat *et al.*, JLab experiment E04-108 (2004).

[43] L. Pentchev *et al.*, LOI-07-013 (2007).

[44] G. Cates *et al.*, JLab experiment E02-013 (2002).

[45] B.Quinn, private communication.